




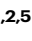

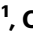




Complementary dual-virus strategy drives synthetic target and cognate T-cell engager expression for endogenous-antigen agnostic immunotherapy

Received: 12 October 2023

Accepted: 9 August 2024

Published online: 23 August 2024

 Check for updates

Zaid Taha ^{1,2,5} , Mathieu Joseph François Crupi ^{1,2,5} , Nouf Alluqmani^{1,2}, Duncan MacKenzie¹, Sydney Vallati^{1,2}, Jack Timothy Whelan^{1,2}, Faiha Fareez³, Akram Alwithenani^{1,2}, Julia Petryk¹, Andrew Chen¹, Marcus Mathew Spinelli¹, Kristy Ng¹, Judy Sobh¹, Christiano Tanese de Souza¹, Priya Rose Bharadwa^{1,2}, Timothy Kit Hin Lee^{1,2}, Dylan Anthony Thomas^{1,2}, Ben Zhen Huang^{1,2}, Omar Kassas¹, Joanna Poutou¹, Victoria Heather Gilchrist^{1,2}, Stephen Boulton ¹, Max Thomson¹, Ricardo Marius¹, Mohsen Hooshyar¹, Scott McComb⁴, Rozanne Arulanandam ¹, Carolina Solange Ilkow^{1,2}, John Cameron Bell ^{1,2,6}  & Jean-Simon Diallo ^{1,2,6} 

Targeted antineoplastic immunotherapies have achieved remarkable clinical outcomes. However, resistance to these therapies due to target absence or antigen shedding limits their efficacy and excludes tumours from candidacy. To address this limitation, here we engineer an oncolytic rhabdovirus, vesicular stomatitis virus (VSV Δ 51), to express a truncated targeted antigen, which allows for HER2-targeting with trastuzumab. The truncated HER2 (HER2T) lacks signaling capabilities and is efficiently expressed on infected cell surfaces. VSV Δ 51-mediated HER2T expression simulates HER2-positive status in tumours, enabling effective treatment with the antibody-drug conjugate trastuzumab emtansine *in vitro*, *ex vivo*, and *in vivo*. Additionally, we combine VSV Δ 51-HER2T with an oncolytic vaccinia virus expressing a HER2-targeted T-cell engager. This dual-virus therapeutic strategy demonstrates potent curative efficacy *in vivo* in female mice using CD3⁺ infiltrate for anti-tumour immunity. Our findings showcase the ability to tailor the tumour micro-environment using oncolytic viruses, thereby enhancing compatibility with “off-the-shelf” targeted therapies.

Precision medicine in the field of antineoplastic therapy focuses on tailoring treatments based on the molecular profiles of diseases. Cancer immunotherapies¹, such as immune checkpoint inhibitors, targeted biologics, and adoptive cell transfers, have emerged as highly targeted systemic therapies with improved efficacy and safety. The success of these therapies relies on the specific molecular targets

expressed by tumours. For example, HER2 amplification, which was originally associated with poor prognoses, now allows for targeted therapies with better outcomes^{2–5}. Indeed, while the frequency of HER2 amplification may be high in some cancers, it may also be low in others thereby imposing a candidacy barrier to potentially curative targeted therapies. We therefore propose a different approach to precision

A full list of affiliations appears at the end of the paper.  e-mail: ztaha053@uottawa.ca; mcrupi@ohri.ca; jbelle@ohri.ca; jsdiallo@ohri.ca

medicine. Instead of customizing the therapy for the tumour, we aim to modify the tumour in situ rendering it compatible with existing targeted biologics.

In this study, we generate VSVΔ51 encoding a truncated version of HER2 (HER2T) that simulates HER2-positive status, but incapable of signalling⁶. HER2 is used here as a proof-of-concept target antigen. Importantly, we show that VSVΔ51-HER2T can be combined with existing HER2-targeted therapy trastuzumab emtansine (Kadcyla®, T-DM1) to treat HER2-negative tumours³. We next designed and encoded a HER2-targeted T-cell engager (TCE) into a second oncolytic virus, vaccinia virus (VV). We have previously demonstrated the advantages of using VV as a delivery platform for TCEs that recognize orthogonal targets in the tumour microenvironment⁷. Here, our dual-virus strategy utilizes VSVΔ51 to deliver a target antigen, while the VV delivers a therapeutic TCE which binds to that same target. We observe curative responses as a result of significant T-cell mediated tumour cell destruction, attributable to the mechanistic synergy between the viral payloads. We moreover demonstrate the rational selection of these two complementary oncolytic viruses, owing to their inherent combinatorial synergy⁸.

In this work, we demonstrate the potential for oncolytic viruses to reshape the molecular profile of tumours, enabling them to become candidates for targeted immunotherapy. These findings have implications in removing molecular barriers to patient access and eligibility for efficacious targeted therapies.

Results

Synthetic HER2T antigen encoded within VSVΔ51 is expressed in vitro and in vivo and can be recognized by trastuzumab

Levels of cell-surface target expression confer sensitivity to targeted biologics, such as the antibody-drug conjugate (ADC) T-DM1⁵. Indeed, HER2-low 786-O cells showed reduced sensitivity to T-DM1 compared to HER2-high AF2068 cells (Supplementary Fig. 1a, b). VSVΔ51 replication was enhanced in AF2068 cells, but not 786-O cells, treated with low concentrations of T-DM1 (Supplementary Fig. 1c), consistent with our previous studies. Here, we encoded a truncated, kinase-dead version of HER2 (HER2T)⁶, retaining the trastuzumab epitope and its ability to simulate HER2+ status, into the VSVΔ51 genome (Fig. 1a). We rescued and purified the oncolytic virus (Fig. 1b), referred to as VSVΔ51-HER2T, which exhibited unchanged growth kinetics relative to control VSVΔ51-Fluc (Supplementary Fig. 1d). HER2T expression peaked at -16 h post-infection (hpi) with VSVΔ51-HER2T in 4T1.2 cells, visualized by immunofluorescence staining (Supplementary Fig. 1e–g). We demonstrated that VSVΔ51-induced HER2T protein trafficked to the cell surface in CT26 and MC38 cells (Fig. 1c). VSVΔ51-HER2T also enhanced trastuzumab binding in HER2-low HT29 cells (Supplementary Fig. 1h) and did not infect normal GM38 fibroblasts to express HER2T (Supplementary Fig. 1i).

We next administered equal doses of intratumoural (i.t.) injections of VSVΔ51-HER2T or VSVΔ51-GFP, into subcutaneous (s.c.) CT26 tumours in wildtype BALB/c mice (Supplementary Fig. 1j). Tumour sections obtained 24 h post-injection revealed HER2T+ trastuzumab-binding only in VSVΔ51-HER2T-treated tumours by immunohistochemistry (Fig. 1d). HER2T+ regions overlapped with VSVΔ51+ regions in these sections, suggesting antigen expression is localized. These data suggest VSVΔ51-HER2T exhibits unimpaired growth kinetics and mediates trastuzumab-binding cell-surface expression of HER2T in vitro and in vivo.

VSVΔ51-mediated HER2T expression sensitizes solid tumours to T-DM1 in murine tumour models in vivo and in patient tumour specimens ex vivo

Our group previously published on the mechanistic synergy between microtubule destabilizing agents (MDAs) and VSVΔ51^{2,6,9}. We found that MDAs enhance VSVΔ51 spread and bystander killing within

tumours, through disruption of type I interferon secretion. We moreover demonstrated that ADCs bearing an MDA payload led to the same combinatorial synergy with VSVΔ51 although in a very specific targeted fashion^{2,6}. To determine whether HER2T can respond to a HER2-targeted therapy, we treated ex vivo murine CT26 tumour cores with VSVΔ51-HER2T and T-DM1 (Supplementary Fig. 2a). CT26 tumour cores were used in ex vivo experiments to refine the treatment conditions before implementing more challenging patient surgically-excised tumour specimens. We demonstrated that viral replication was enhanced in a HER2T-dependent manner (Supplementary Fig. 2b), consistent with previous findings showing increased VSVΔ51 replication in the presence of T-DM1 in HER2+ cell lines^{2,6,9}. Similar results were observed in patient tumour cores (Fig. 1e, f; Supplementary Fig. 2c; Supplementary Table 1). Briefly, patient tumours were treated with VSVΔ51-HER2T + T-DM1 (Fig. 1e, f), or VSVΔ51-GFP + T-DM1 as control (Supplementary Fig. 2c, Supplementary Table 1). Viral titres were only enhanced in the presence of VSVΔ51-induced HER2T, which enabled binding of T-DM1 and its subsequent internalization, leading to enhanced VSVΔ51 output. In the control condition using VSVΔ51-GFP, there was no target for T-DM1 to bind to, and therefore there was no enhancement of VSVΔ51 output.

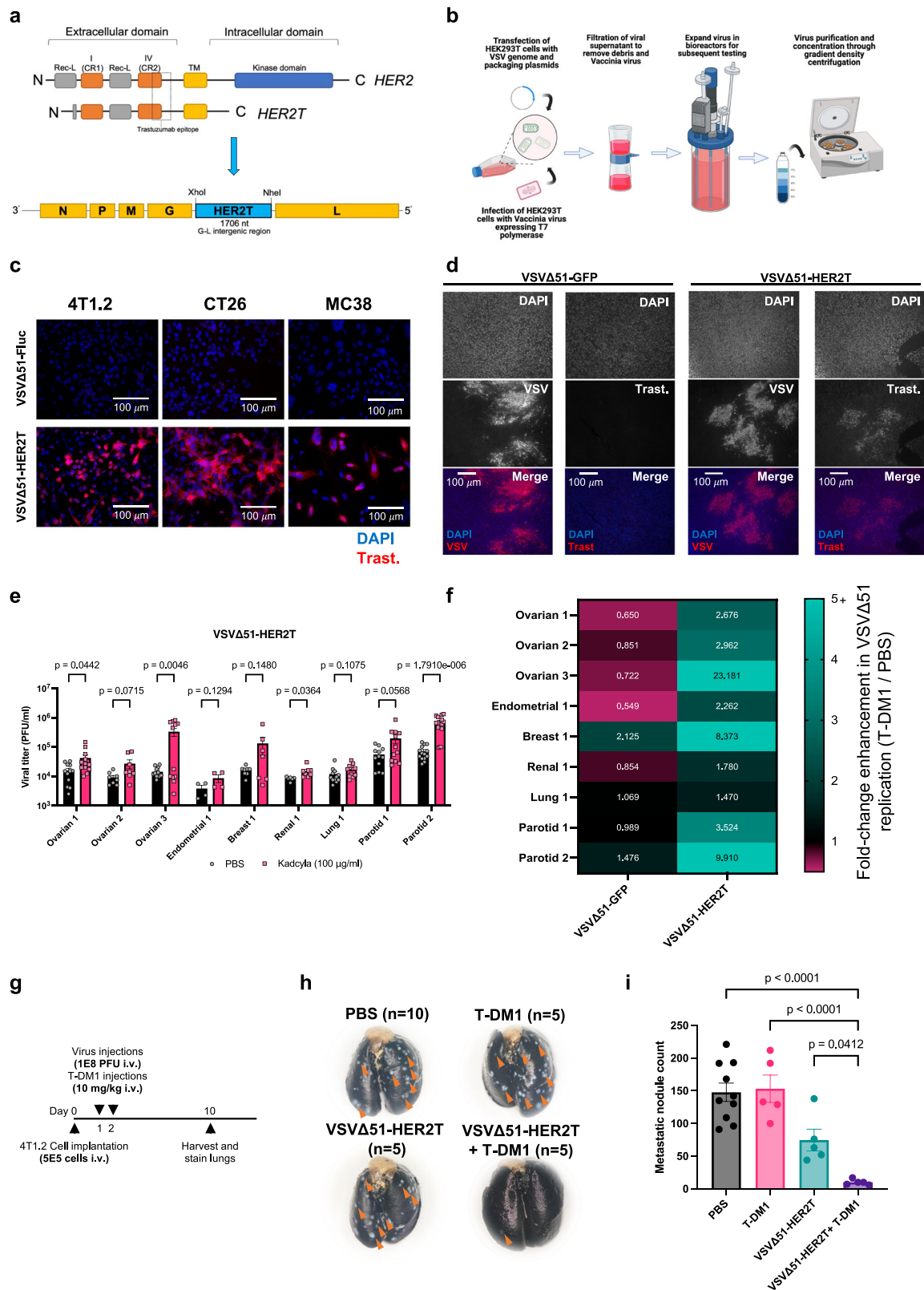
In vivo, we utilized a disseminated disease model based on intravenous (i.v.) implantation of the 4T1.2 murine mammary carcinoma model and i.v. treatments^{6,10,11} (Fig. 1g). We previously optimized this model⁶, and here we confirmed that following i.v. injection of cells stained with an infrared dye, cells can be detected in the lungs of the animals at 1 h and 24 h post-injection by fluorescence IVIS imaging (Supplementary Fig. 3a–d). Indeed, histological assessment of lungs harvested 24 h post-injection of cells revealed presence of micro-metastatic lesions (Supplementary Fig. 3e, f). More specifically, we observed foci within regions of interest, containing large epithelioid cells with ample eosinophilic cytoplasm, high nuclear:cytoplasmic ratio, prominent nucleoli, open vesicular chromatin and pleomorphism. These findings confirm the presence of established lung metastases before treatment initiation.

Implementing this validated model for assessment of our therapeutic strategy, we observed a reduction in lung tumour nodules following combination treatment with VSVΔ51-HER2T and T-DM1 (Fig. 1h, i). We further assessed this combination approach in a disseminated disease model of ovarian high-grade serous carcinoma bearing *Tp53* and *Pten* double knockouts (ID8-PP) (Supplementary Fig. 4a–c) and in a subcutaneous MC38 murine colorectal carcinoma tumour model (Supplementary Fig. 4d–g). The combination treatment stunted tumour progression and improved overall survival in these ovarian and colorectal carcinoma models (Supplementary Fig. 4a–f). Importantly, the therapeutic regimen was well-tolerated (Supplementary Fig. 4g). Together, these findings suggest that VSVΔ51-HER2T delivers a surface antigen that enables targeting of infected tumour cells by clinically-approved T-DM1. This combination enables utilization of HER2-targeted biologics^{2,3,5,6,9} in HER2-negative tumours, including clinical tumour specimens.

HER2T-targeted TCEs activate T-cells and can be encoded in oncolytic VV

Having demonstrated compatibility between VSVΔ51-HER2T and an “off-the-shelf” therapeutic as a proof-of-concept, we next evaluated a second approach using a dual-virus combination strategy. As rationale, we have previously demonstrated the anti-tumour synergy of VSVΔ51 and VV in human cancer cell lines and the potent effects of picomolar amounts of TCE produced by VV^{7,8}, highlighting the potential for payload-mediated mechanistic synergy.

First, we engineered a HER2-targeted T-cell engager (TCE) (Fig. 2a). The TCE, designed with trastuzumab single-chain variable fragments (scFv) targeting human HER2 and either mouse or human CD3ε, was validated for secretion and binding to HER2+ cell lines



(Fig. 2b–d, Supplementary Fig. 5a, b). Herein, “Ctrl-TCE” designation will refer to the αHER2-TCE bearing the incompatible αCD3ε species arm as a negative control in experiments. Notably, the TCE exhibited binding, similar to trastuzumab, on MC38-HER2T cells (Fig. 2e, f). T-cell stimulatory activity of the αHER2-TCE was confirmed through co-culture experiments, using HER2+ human ovarian cancer cell lines or HER2T+ ID8 murine ovarian cancer cells, with Jurkat cells expressing TdTomato under the control of the CD69 promoter (J69)⁷ (Fig. 2g). The

presence of αHER2-TCE led to increased TdTomato signal of J69 cells in co-culture with cells expressing HER2 or HER2T. The αHER2-TCE was further shown to induce target-dependent cytolytic activity by reducing the viability of HER2+ or HER2T + 4T1.2 target cells in the presence of naïve syngeneic splenocytes (Fig. 2h), with no impact on HER2- cells.

Next, we successfully encoded the TCEs into vaccinia virus (VV), which we rendered oncolytic by J2R deletion (Fig. 2i), and then

Fig. 1 | VSVΔ51-encoded HER2T is expressed in vitro and in vivo. **a** Schematic of the HER2T construct encoded within VSVΔ51. **b** Overview of VSVΔ51 rescue, propagation, and purification. **c** 4T1.2, CT26, and MC38 cells were seeded on glass coverslips and infected with the indicated VSVΔ51 variants at MOI 0.1 and incubated for 20 h. Cells were fixed in 4% paraformaldehyde (PFA) and stained using trastuzumab as a primary antibody (1:1000) and goat anti-human IgG-Alexa Fluor 594 (1:300) as a secondary antibody. Cells were mounted using ProLong Gold Antifade with DAPI, and imaged at 20× magnification using a Zeiss AxioImager M1. Similar results were seen across 3 different independent experiments. **d** Tumour samples were stained using trastuzumab as a primary antibody (1:1000), and goat anti-human IgG-Alexa Fluor 594 (1:300) as a secondary antibody. Sections were mounted using Prolong Gold Antifade with DAPI. Sections were imaged using the Zeiss AxioImager M1 at 10× magnification. Similar results were seen across 3 different independent experiments. **e, f** Patient tumour cores were infected with (e) VSVΔ51-HER2T and co-treated with T-DMI or mock (PBS) as indicated. Viral titre in

supernatants was quantified 48 hpi. Shown are mean ± SEM, $n = 4$ –14 cores, P -value calculated by multiple unpaired t -tests. (Endometrial 1 $n = 4$, Renal 1 $n = 6$, Ovarian 2 and Breast 1 $n = 8$, Parotid 2 $n = 14$, all others $n = 12$). **f** Ratios of mean viral titre of T-DMI/PBS for samples infected with VSVΔ51-HER2T or VSVΔ51-GFP were calculated and plotted as a heat map. **g** Experimental overview: 5×10^5 4T1.2 cells were injected i.v. by tail vein injection into wildtype BALB/c mice on D0 and then treated on D1 and D2 by i.v. administration of PBS, VSVΔ51-HER2T, T-DMI, or VSVΔ51-HER2 + T-DMI. Mice were euthanized on D10 post-implantation, and lungs were extracted, perfused, and stained for counting of metastatic lung nodules. **h** Following staining with black India ink, lungs were fixed and imaged. **i** Lung nodules from **g** and **h** were counted. Shown are mean ± SEM, $n = 10$ mice in PBS, $n = 5$ mice in treatment groups, P -value calculated by one-way ANOVA relative to PBS, with Dunnett correction for multiple comparisons. Source data are provided as a Source Data file.

confirmed that VV- α HER2-TCE maintained viral growth kinetics comparable to VV-Ctrl-TCE using growth curves and immunoblotting (Fig. 2j, k). The selection of VSVΔ51 and VV as complementary viral vectors for delivering HER2T and cognate TCE payloads was motivated by their observed feed-forward synergy (Supplementary Fig. 6). VSVΔ51, susceptible to IFN β -mediated antiviral effects, showed improved replication and spread when co-infected with VV, particularly in the presence of high IFN β concentrations (Supplementary Fig. 6a–d). The combination also resulted in enhanced VSVΔ51 replication in VSVΔ51-resistant cell lines expressing endogenous IFN β (Supplementary Fig. 6c, d). We gauged the biodistribution of i.t. administered dual viruses in CT26 tumour-bearing BALB/c mice, where we observed minimal or non-detectable VSVΔ51 in off-target organs at 48 h post-injection (Supplementary Fig. 6e). We moreover observed increased *VSV-N* transcripts in tumours where VSVΔ51 was co-administered with VV, suggesting enhanced VSVΔ51 replication, likely attributable to the synergy between the two viruses. These findings indicated that a low threshold of VV infection, as observed in murine cancer cell lines, was sufficient for therapeutic efficacy, supporting the minimal requirement for VV tumour infection (Supplementary Fig. 6d). In summary, we confirmed the functional engagement of the engineered α HER2-TCE with HER2T and its successful incorporation into VV, reinforcing the potential of the VSVΔ51-HER2T and VV-TCE combination for a feed-forward anti-tumour response.

Treatment of murine HER2T tumour models with VV- α HER2-TCE leads to efficacy in vivo

Efficacy of VV- α HER2-TCE was assessed in murine models of HER2T+ cancer, including 4T1.2-HER2T (Supplementary Fig. 7a–f) and CT26-HER2T (Supplementary Fig. 7g–l) s.c. tumour models and i.p. ID8-PP-HER2T tumour model (Supplementary Fig. 7m, n). Treatment of 4T1.2-HER2T tumour-bearing mice with VV- α HER2-TCE resulted in significant tumour growth stunting (Supplementary Fig. 7b) and improved overall survival compared to controls (Supplementary Fig. 7c), with tolerable treatments and stable weights (Supplementary Fig. 7d). Complete tumour regression was observed in 2/5 mice (40%), and rechallenge experiments confirmed tumour rejection (Supplementary Fig. 7e, f). Similar results were observed in the CT26-HER2T model, with safe administration, reduction in tumour progression and enhanced overall survival (Supplementary Fig. 7h–j), and complete tumour rejection upon rechallenge (Supplementary Fig. 7k, l). In the i.p. ID8-PP-HER2T model, VV- α HER2-TCE significantly improved overall survival compared to control groups (mOS 50 days vs 28–33 days) (Supplementary Fig. 7m, n). These findings underscore the therapeutic efficacy afforded by α HER2-TCE in murine tumour models expressing the same HER2T antigen encoded within VSVΔ51-HER2T, supporting the use of the latter in localized and disseminated tumour models.

Treatment of murine and patient tumours ex vivo with VSVΔ51-HER2T and VV- α HER2-TCE combination leads to T-cell activation

Having demonstrated that the HER2T antigen engages VV-encoded α HER2-TCE in vivo, we next evaluated the ability of the virally-encoded TCE to engage and induce T-cell activation. For this ex vivo approach, we first obtained MC38-HER2T tumour cores by punch biopsy (Supplementary Fig. 8a, b). These tumour cores were incubated with J69 cells alone, or in combination with VV-Ctrl-TCE or VV- α HER2-TCE (Supplementary Fig. 8c). Flow cytometric quantification of J69 signal 48 hpi revealed a significant enhancement in the total frequency and signal intensity of activated J69 cells (Supplementary Fig. 8d–f). Having optimized conditions, we implemented a similar approach using wildtype HER2- MC38 tumour cores co-infected with VSVΔ51-HER2T and VV- α HER2-TCE (Fig. 3a–e, Supplementary Fig. 8g). Flow cytometric quantification of J69 cells revealed a robust CD69-TdTomato signal 48 hpi following co-infection with VSVΔ51-HER2T and VV- α HER2-TCE compared to control virus combinations (Fig. 3b, c). This effect was reproducible in CT26 tumour cores, another HER2-negative murine model (Fig. 3d, e).

We observed similar outcomes in human HER2-low HT-29 colorectal tumour cores from xenografts (Fig. 3f, g). Quantification of J69 TdTomato signal reveals significant activation following co-infection with VSVΔ51-HER2T and VV- α HER2-TCE compared with all other conditions. These findings demonstrated using HT-29 cores are especially important, as HT-29 cells express low-intermediate levels of HER2 (Supplementary Fig. 8h). These data therefore suggest this approach is viable in both HER2- tumours to introduce the target antigen, or in HER2-low tumours to increase pre-existing antigen density for improved targeting. Indeed, we induced significant enhancement in J69 activation 48 hpi following co-infection of patient tumour cores with VSVΔ51-HER2T and VV- α HER2-TCE (Fig. 3h; patient clinical characteristics Supplementary Table 2) relative to other conditions.

Taken together, these findings suggest that this combination approach induces target-directed T-cell activation in HER2-negative, -low, and -high ex vivo tumours. Importantly, this activation is reliant upon target expression for the full impact of TCE activity. Finally, TCE-induced T-cell activation in target-low tumours can be further enhanced following target-upregulation through VSVΔ51-HER2T.

Co-administration of VSVΔ51-HER2T and VV- α HER2-TCE in vivo leads to improved survival in localized models of disease

After confirming the biological activity of our TCE both in vitro and in vivo, and compatibility with the HER2T antigen, we next assessed our dual-virus approach in multiple HER2-negative in vivo syngeneic tumour models. We first assessed the response of our combination therapeutic strategy in MC38 s.c. tumours (Fig. 4a). Mice were treated with VV- α HER2-TCE alone, or a combination of VV and VSVΔ51 with different permutations of transgenes to ensure equivalent total viral dose, of which only the combination of VSVΔ51-HER2T+VV- α HER2-TCE

Fig. 2 | Engineered α HER2-TCE recognizes HER2T antigen and can be encoded in VV. **a** Schematic of the anti-HER2 TCE design. **b** TCE expression plasmids were transfected into HEK293T cells, and supernatants were resolved by SDS-PAGE 48 h post-transfection. Blots were probed with anti-His antibody to detect His-tagged TCEs. Similar results were seen across 3 different independent experiments. **c** Whole cell lysates of the indicated cell lines were resolved by SDS-PAGE and probed with anti-HER2 antibody. **d** TCE binding assay for the indicated cell lines (mean \pm SEM, $n = 3$, P -value calculated by two-way ANOVA with Sidak's correction for multiple comparisons). **e, f** trastuzumab and TCE binding assays for MC38 and MC38-HER2T. (mean \pm SEM, $n = 3$). **g** J69 cells (1×10^6) were co-cultured for 24 h with the indicated cell lines (5×10^5) in the presence or absence of 10 μ g/ml α HER2-TCE. J69 cells were then dislodged and isolated and TdTomato signal was quantified by the BioTek Cytation5 (Gen5 v2 software) at Ex_{555nm}/Em_{580nm} (mean \pm SEM, $n = 3$, P -value calculated by multiple unpaired t-tests with the Holm-Sidak correction for multiple comparisons.) **h** Naïve BALB/c splenocytes were isolated and co-cultured with the indicated target cells at a T:E ratio of 1:0 or 1:5. Co-cultures were incubated for 72 h with or without 10 μ g/ml α HER2-TCE. Cell viability

was assessed by AlamarBlue and normalized to untreated target cells alone (mean \pm SEM, $n = 3$, P -value calculated by multiple unpaired t-tests with the Holm-Sidak correction for multiple comparisons.) **i** Schematic of the engineering of TCEs into VV and subsequent viral rescue and purification. **j** Multi-step (left, MOI 0.01) and single-step (right, MOI 1.0) VV growth curves. U-2 OS cells were seeded in 6-well plates at 1×10^6 cells per well and incubated overnight. Cells were infected with VV-Ctrl, VV-Ctrl-TCE, or VV- α HER2-TCE at the indicated MOI, and frozen at -80°C at the indicated timepoints. Cells undergo a total of 3 freeze-thaw cycles to liberate intracellular VV, which was subsequently quantified by plaque assay. Shown are mean \pm SEM, $n = 3$, P -value calculated by two-way ANOVA with Tukey's correction for multiple comparisons. * $P < 0.05$, *** $P < 0.001$, relative to VV- α HER2-TCE. (P -values resulting from the two-way ANOVA are included in the Source Data file for this figure). **k** Whole cell lysates of U-2 OS cells infected with VV and resolved by SDS-PAGE. Blots were probed with anti-His IgG to quantify His-tagged TCE, and anti-Vaccinia IgG to confirm VV infection. Similar results were seen across 3 different independent experiments. Source data are provided as a Source Data file.

With the previous two models being in situ tumours, we next treated BALB/c mice bearing metastatic 4T1.2 s.c. tumours (Fig. 4k–m). We observed that 5/5 mice treated with VSV Δ 51-HER2T+VV- α HER2-TCE exhibited significant stunting in tumour progression (Supplementary Fig. 9e), which led to a significant enhancement in overall survival compared to controls (mOS 57 days vs 32–39 days), and all treatments were well-tolerated (Supplementary Fig. 9f).

To evaluate the extent of tumour control our dual-virus combination exerts, we implemented a single-shot approach for subsequent immunological studies and disseminated disease models. We optimized a co-formulated dose containing both OVVs and verified that this co-formulation yields similar efficacy to our original sequential treatment regimen (Supplementary Fig. 10a–d). This co-formulation enables a more rapid treatment administration within a shorter timeframe to allow the assessment of intratumoural immune responses at early timepoints. We moreover demonstrated that switching the order of the OVVs in the sequential regimen does not significantly impact efficacy (Supplementary Fig. 10c).

We next examined the extent of viral infection within injected tumours following a single co-formulated injection, to validate successful tumour infection (Supplementary Fig. 11). BALB/c bearing CT26 tumours were injected intratumourally as indicated (Supplementary Fig. 11a). Tumours were harvested at 24 or 48 hpi then dissociated and interrogated by flow cytometry for the quantification of virus-infected tumour cells (Supplementary Fig. 11b–f). We report that approximately 2% of tumour cells were infected by VSV Δ 51-HER2T, increasing to ~4% when co-injected with VV, at both 24 and 48 hpi (Supplementary Fig. 11b, c). VV infected 0.1–1% of tumour cells, increasingly modestly when co-injected with VSV Δ 51-HER2T (Supplementary Fig. 11d, e). We also observed a reduced proportion of VSV Δ 51-HER2T+VV- α HER2-TCE co-infected cells, compared to VSV Δ 51-HER2T+VV-Ctrl-TCE. Examination of tumours by IHC confirms presence of VSV Δ 51-HER2T and VV (Supplementary Fig. 11g, h), with a notable enhancement in VSV Δ 51-HER2T spread in tumours injected with VSV Δ 51-HER2T+VV (Supplementary Fig. 11g). Quantification of the total VSV Δ 51-positive area in all tumours confirms a significant enhancement of VSV Δ 51-HER2T staining when combined with VV in vivo.

To assess immediate virus-induced oncolysis following treatment as indicated (Supplementary Fig. 11a), we examined tumours 48 hpi by immunohistochemical evaluation to determine levels of two markers of cell death: cleaved caspase-3 and 1. Here, we focused on the analysis of regions of interest (ROI) exhibiting robust positive staining for VSV Δ 51-HER2T and VV (Supplementary Fig. 12a) to determine the percentage of cells staining positive for cell death markers. Examination of these ROI as indicated (Supplementary Fig. 12a) reveal increased percentage of cleaved caspase-3 positive cells (Supplementary Fig. 12b) and cleaved caspase-1 positive cells (Supplementary

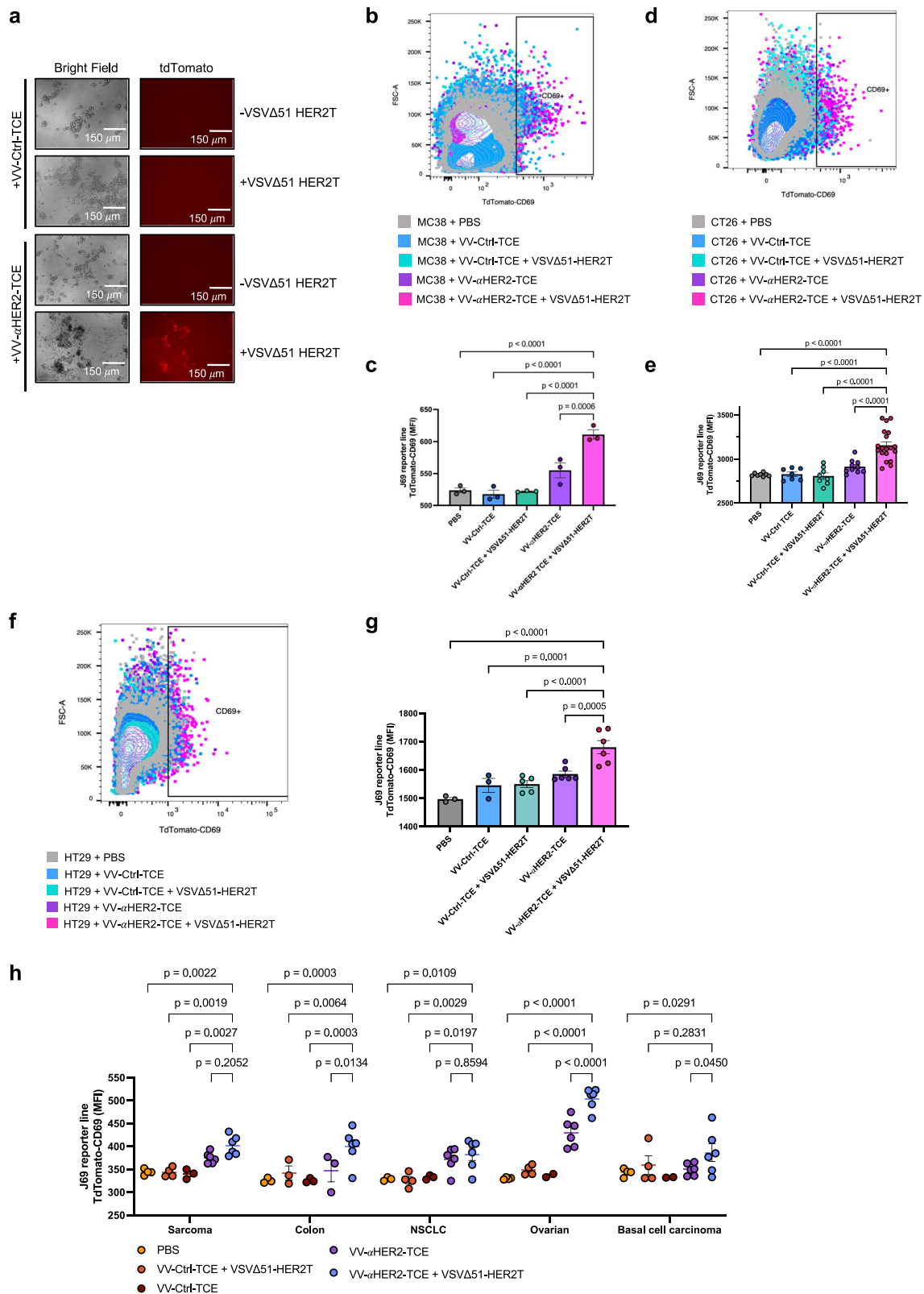
Fig. 12c) in tumours injected with VSV Δ 51-HER2T+VV- α HER2-TCE, compared with control groups.

These data taken together confirm that viral infection following injection is successful and detectable until at least 48 hpi. Highly infected intratumoural foci exhibited elevated proportions cells staining positive for cell death markers. The total proportion of the tumour infected by either VSV Δ 51-HER2T or VV- α HER2-TCE was estimated to be approximately 1–4%, as confirmed by both flow cytometry and IHC. This minor infection rate suggests that the overall efficacy of the dual-virus injection we previously observed likely involves the triggering of a significant anti-tumour immune response. Therefore, we next aimed to characterize early and late anti-tumour immune responses.

Treatment of tumour-bearing mice with VV- α HER2-TCE and VSV Δ 51-HER2T enhances tumour-infiltrating lymphocyte activation and migration in the tumour

Having established efficacy of our single-shot, dual-virus approach in multiple tumour models, we aimed to verify the early immune mechanisms by which the viral payloads operate. Dual-virus treatment of subcutaneous CT26 tumours with VV- α HER2-TCE+VSV Δ 51-HER2T resulted in increased IFN γ + and TNF α + tumour-infiltrating lymphocyte (TIL) populations (Fig. 5a–d) at 72 hpi, consistent with TCE-mediated T-cell activation^{12,13}. These TILs include CD4+, CD8+, and invariant TCR $\gamma\delta$ CD3+ T-cells, all of which exhibited reactivity against irradiated CT26 tumour cells and irradiated HER2 + JIMT1 cells¹⁴, with elevated baseline (PBS) activity (Fig. 5b–d).

Profiling of T-cell and NK responses at day 5 post-treatment revealed a distinct shift in the clustering patterns of these lymphocytes following treatment with VV- α HER2-TCE+VSV Δ 51-HER2T (Fig. 5e–g, Supplementary Fig. 13a–g, Supplementary Fig. 14a, b). Interrogation of the optimized t-distributed stochastic neighbour embedding (opt-SNE)¹⁵ plots revealed hot-spots of migratory CXCR3+ lymphocytes following combination treatment, absent in control groups. Indeed, VV- α HER2-TCE+VSV Δ 51-HER2T treatment upregulated migratory marker CXCR3 in CD3+ TILs (Fig. 5e), including CD4+, CD8+, TCR $\gamma\delta$ T-cells and NK cells (Supplementary Fig. 13b–e). We moreover observed a trend towards reduced CD3 ϵ expression (Supplementary Fig. 13f), suggestive of early T-cell activation associated with TCEs^{12,13}. Exhausted T-cell phenotypes (PD1+LAG3+) were also reduced following combination treatment, along with immune-suppressive CTLA4+ T_{reg} populations and PD-L1+ macrophages (Fig. 5f, g, Supplementary Fig. 13g). These results indicate an enhanced migratory potential of TILs and reduced immune suppression in the tumour microenvironment immediately following intratumoural injection of VSV Δ 51-HER2T and VV- α HER2-TCE. These data highlight the early signs of mechanistic synergy of the viral payloads in mediating efficacy.



We next aimed to assess systemic immune responses following therapy, including directly anti-tumour immune responses as well as anti-viral and anti-HER2T immune responses. Following intratumoural injection of BALB/c mice bearing s.c. CT26 tumours as indicated (Fig. 5h), serum was isolated from peripheral blood at D7 and D14 post-treatment and spleens were harvested at D14 post-treatment.

Splenocytes isolated at D14 were assessed for antigen reactivity by ELISpot (Fig. 5i–m, Supplementary Fig. 15a) and by intracellular

cytokine staining (ICS) (Supplementary Fig. 15b–h). Splenocytes isolated from mice that received VSVΔ51-HER2T and VV-αHER2-TCE treatment exhibited significantly increased reactivity against a specific CT26-derived tumour antigen (gp70, Fig. 5i) or tumour cells (irrCT26, Fig. 5j), compared with control groups. This same treatment group also exhibited significant reactivity against HER2+ JIMT1 cells, indicative of reactivity against the exogenous HER2T antigen (Fig. 5k). Anti-viral responses against VSVΔ51 or VV were only detectable in groups

Fig. 3 | Infection of tumours with VV- α HER2-TCE ex vivo leads to T-cell activation when combined with VSV Δ 51-HER2. **a** Images acquired using the EVOS M5000 microscope of the co-cultured J69 cells, which were cultured with MC38 tumour cores under different treatment conditions as indicated (20 \times magnification) **b** J69 cells from **a** were isolated and assessed for TdTomato signal by flow cytometric analysis. **c** MFI of TdTomato+ J69 cells was quantified. Shown are mean \pm SEM, $n = 3$ cores per group; P -value calculated by one-way ANOVA, with Dunnett correction for multiple comparisons. **d** J69 cells were isolated from co-culture with CT26 tumour cores following treatment as indicated, and TdTomato signal was quantified by flow cytometric analysis. **e** Quantification of TdTomato signal from **d**. Shown are mean \pm SEM, $n = 6$ –19 cores per group; P -value calculated by one-way ANOVA related to VSV Δ 51-HER2T+VV- α HER2-TCE, with Dunnett correction for multiple comparisons. PBS $n = 8$, VV-Ctrl-TCE $n = 7$, VV-Ctrl-TCE

+VSV Δ 51-HER2T $n = 8$, VV- α HER2-TCE $n = 10$, VV- α HER2-TCE+VSV Δ 51-HER2T $n = 19$). **f** HT29 xenografts were excised and cored by punch biopsy, then treated and co-cultured with J69 cells. J69 cells were isolated and assessed for TdTomato signal by flow cytometric analysis. **g** Quantification of TdTomato signal from **f**. Shown are mean \pm SEM, $n = 3$ –6 cores per group; P -value calculated by one-way ANOVA related to VSV Δ 51-HER2T+VV- α HER2-TCE, with Dunnett correction for multiple comparisons. (PBS $n = 3$, VV-Ctrl-TCE $n = 3$, VV-Ctrl-TCE+VSV Δ 51-HER2T $n = 5$, VV- α HER2-TCE $n = 6$, VV- α HER2-TCE+VSV Δ 51-HER2T $n = 6$). **h** Patient tumour specimens were treated and analysed for J69 TdTomato signal. Shown are mean \pm SEM, $n = 2$ –6 cores per group (for exact n values, see Source Data); P -value calculated by one-way ANOVA related to VSV Δ 51-HER2T+VV- α HER2-TCE within each specimen, calculated only for $n = 3$ or more cores. Source data are provided as a Source Data file.

receiving the viral injection (Fig. 5l–m). However, anti-VSV reactivity was significantly higher in the mice receiving dual-virus injections compared to mice receiving VSV Δ 51-HER2T alone, likely a result of the elevated intratumoural VSV Δ 51-HER2T replication and spread due to the presence of VV (Fig. 5l). We further note that anti-gp70 and anti-JIMT1 reactivity was greater, on average, in the VSV Δ 51-HER2T+VV- α HER2-TCE treatment group compared to anti-viral responses (Fig. 5i, k, l, m). Similar reactivity trends were observed by ICS when evaluating the level of IFN γ +CD8+ T-cells following stimulation (Supplementary Fig. 15b–h).

We further assessed the presence of humoral anti-tumour or anti-HER2T responses at D7 and D14 post-treatment (Supplementary Fig. 16). We observed elevated levels of CT26-reactive serum IgG at D7 and D14 post-treatment in mice that received VSV Δ 51-HER2T and VV- α HER2-TCE injections; CT26-reactive IgG reached levels significantly greater than those detectable in control groups by D14 (Supplementary Fig. 16a–e). Similar evaluation of HER2-reactive IgG revealed a significant elevation in the serum of mice treated with VSV Δ 51-HER2T and VV- α HER2-TCE at D7 post-treatment compared to all control groups (Supplementary Fig. 16f, g). Modest elevations at this timepoint were also detected in the control groups receiving VSV Δ 51-HER2T compared to PBS. By D14 post-treatment all HER2-reactive IgG reached comparable levels (Supplementary Fig. 16i, j).

Taken together, these data indicate that intratumoural VSV Δ 51-HER2T+VV- α HER2-TCE injections induce early activation and migration of immune subsets into tumours within 3–5 days post-treatment. Evaluation of systemic immune responses at a late timepoint, D14 post-treatment, revealed robust anti-tumour immune cellular and humoral responses. We also observed anti-viral responses at D14, include those reactive against the VSV Δ 51-delivered HER2T.

Co-administration of VSV Δ 51-HER2T and VV- α HER2-TCE in vivo leads to improved survival and reduced metastases in disseminated models of disease

Having validated the presence of robust systemic anti-tumour immune responses following intratumoural injections (Fig. 5), we postulated that these same systemic immune responses can confer therapeutic benefit in disseminated disease models. To address this hypothesis, we first treated BALB/c mice bearing the 4T1.2 lung metastases model (Fig. 6a–c). We observed no impact following treatment with VV alone, relative to PBS control. Treatment with VSV Δ 51-HER2T led to a ~50% reduction in nodule count relative to PBS or VV alone, irrespective of the TCE payload. Treatment with control combinations of VSV Δ 51+VV led to a significant ~70% reduction in nodules relative to PBS control, or a ~60% reduction compared to VSV Δ 51-HER2T alone, underscoring the existing synergy between the two viruses and the rationale for combining VV and VSV Δ 51⁸. Treatment with VSV Δ 51-HER2T+VV- α HER2-TCE led to a significant 93% reduction in nodule count relative to PBS control, and an 85% reduction relative to VSV Δ 51-HER2T alone.

The lung metastasis model demonstrated efficacy of our strategy in early-stage disseminated disease, but it does not capture the true

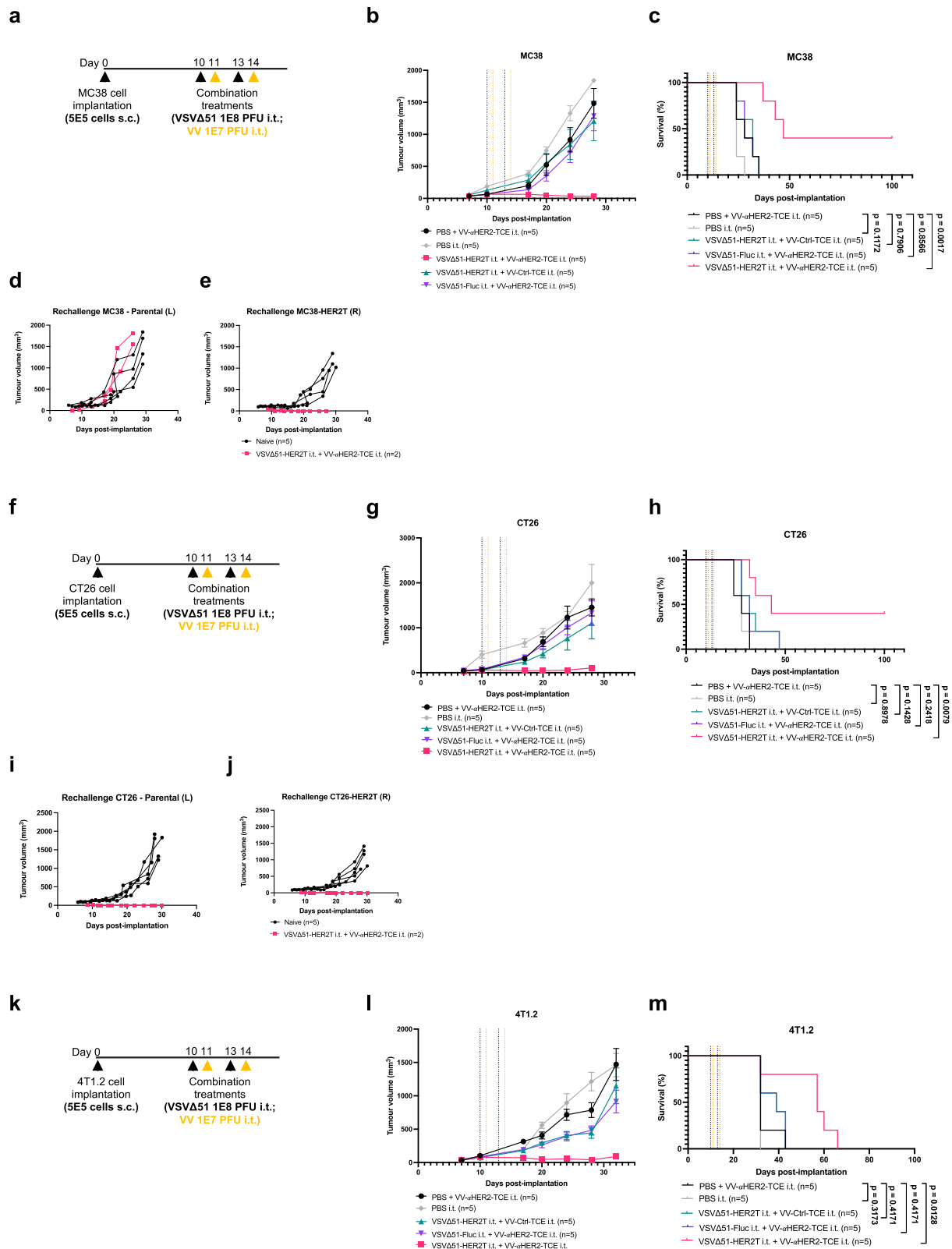
progression of metastasis over time. We therefore further evaluated the therapeutic benefit of the VSV Δ 51-HER2T+VV- α HER2-TCE combination strategy in a post-surgical B16-F10 metastasis model. Briefly, C57BL/6 mice were implanted orthotopically with B16-F10 metastatic melanoma tumours. Tumours were surgically excised at 10 days post-implantation upon reaching ~250 mm³. Treatments were administered intravenously as indicated (Supplementary Fig. 17a) 48 h post-surgery. Mice were monitored up to day 35 post-surgery, upon which the recurrence of the primary tumour was noted and mice were dissected to determine the occurrence of metastases within spleens and lungs (Supplementary Fig. 17b, c). Here we demonstrated that post-surgical systemic treatment with VSV Δ 51-HER2T+VV- α HER2-TCE completely prevented metastases and the recurrence of primary tumours in all mice, while no control treatments led to consistent and significant therapeutic benefit.

We next evaluated the dual-virus approach in ID8-PP i.p. tumours in C57BL/6 mice (Fig. 6d, e). We observed significant improvement in overall survival following systemic treatment with VSV Δ 51-HER2T+VV- α HER2-TCE (mOS 41 days), while treatment with control combinations did not significantly impact survival compared to PBS or monotherapy controls. These findings highlight the robust therapeutic efficacy of our dual-virus approach (Fig. 6f), which confers survival advantage in both metastatic and non-metastatic localized primary tumours, or disseminated disease models. As well, the dual-virus approach offers protection from primary tumour recurrence and metastases when administered in the adjuvant setting following surgical excision of the primary tumour. Finally, both localized or systemic administration of VSV Δ 51-HER2T+VV- α HER2-TCE demonstrated efficacy across colorectal, ovarian, breast, and melanoma preclinical cancer models.

Discussion

In this study, we developed a dual-virus approach to circumvent the restrictive nature of the precision medicine paradigm¹⁶. We encoded a HER2T antigen into oncolytic VSV Δ 51 (Fig. 1) and a complementary TCE into oncolytic VV (Fig. 2). The objective was to elicit a feed-forward anti-tumour immune response that is not dependent on pre-existing tumour antigen expression, overcoming the issue of tumour antigen escape or absence¹⁷. While the use of oncolytic VV^{18,19} or herpes simplex virus²⁰ to deliver CD19 coupled with anti-CD19 CAR T therapy is effective and other universal approaches have been recently reported²¹, CAR T manufacturing leads to lengthy vein-to-vein time, and this waiting period contributes to disease progression and consequently dangerous states of mental health for cancer patients²².

Here, we utilized HER2T⁶ as a target antigen, as we had previously demonstrated synergy between HER2-targeted ADC, T-DM1, and VSV Δ 51^{2,6,9}. Our work showed that T-DM1 enhanced VSV Δ 51 spread and bystander killing in HER2+ tumours due to the mechanistic synergy between VSV Δ 51 and the microtubule destabilizer payload DM1. Indeed, here we further demonstrated efficacy following combination treatment of localized or disseminated tumours with VSV Δ 51-HER2T and T-DM1, in HER2-negative tumour



models and clinical specimens (Fig. 1). These data are important as we showed efficacious combination between a virus-encoded target and a clinically-approved anti-HER2 ADC. The use of the trastuzumab epitope was practical due to its accessibility and the availability of trastuzumab-based therapeutics⁵; trastuzumab deruxtecan (Enhertu®) could be used as an alternative ADC in our regimen as it continues to demonstrate clinical success^{4,23–25}. Of note, this approach can also be extended to any target antigen, including

synthetic or exogenous proteins, with a preference for a synthetic antigen²⁶ to minimize on-target off-tumour effects.

We recognize that there is a possibility of some VSV-infected cells to undergo oncolysis and become eliminated, before antibody recognition of the HER2T. However, VSV-refractory cells can become non-permissively infected without undergoing lysis, making them good candidates for this strategy as they would become tagged with HER2T for targeting. Additionally, VSV-sensitive cells infected with

Fig. 4 | Treatment of tumour-bearing mice with VV- α HER2-TCE and VSV Δ 51-HER2T prolongs overall survival in localized disease models. **a** Experimental overview: 5×10^5 MC38 cells were implanted s.c. in C57BL/6 mice in the right flank. Mice were treated i.t. as indicated. **b** Tumour volumes (mean \pm SEM, $n = 5$ per group) and **(c)** overall survival were monitored (**d, e**). Cured mice from **a–c** were rechallenged with bilateral s.c. tumours, **d** parental MC38 (left flank) or **e** MC38-HER2T (right flank). Naïve mice were challenged with bilateral s.c. tumours in parallel as controls. **f** Experimental overview: 5×10^5 CT26 cells were implanted s.c. in BALB/c mice in the right flank. Mice were treated i.t. as indicated. **g** Tumour

volumes (mean \pm SEM, $n = 5$ per group) and **h** overall survival were monitored. **i, j** Cured mice from **f–h** were rechallenged with bilateral s.c. tumours, **i** parental CT26 (left flank) or **j** CT26-HER2T (right flank). Naïve mice were challenged with bilateral s.c. tumours in parallel as controls. **k** Experimental overview: 5×10^5 4T1.2 cells were implanted s.c. in BALB/c mice in the right flank. Mice were treated i.t. as indicated. **l** Tumour volumes (mean \pm SEM, $n = 5$ per group) and **m** overall survival were monitored. **c, h, m** For analysis of survival data, *P*-values were calculated by the Kaplan–Meier method followed by log-rank test. Source data are provided as a Source Data file.

VSV Δ 51-HER2T express high levels of surface HER2T within 8–16 hpi and before undergoing complete lysis (Supplementary Fig. 1e, f). These timeframes therefore explain the efficacy we observe in vivo as a result of successful HER2T tagging and subsequent TCE or T-DM1 binding (Figs. 1g–i, 4 and 6). Indeed we detected VSV Δ 51-HER2T+ cells in CT26 tumours at both 24 and 48 hpi following in vivo intratumoural injections, by both flow cytometric analysis or IHC (Supplementary Fig. 1i), confirming persistence of VSV Δ 51-infected HER2T-tagged cells.

Our group has previously demonstrated the oncolytic viruses, including VSV and VV, can infect and disrupt tumour vasculature^{27–29}. As a result, tumour delivery of systemically-administered therapies such as T-DM1 (Fig. 1, Supplementary Figs. 1–4) may be hindered in certain situations. To address this potential hurdle, we devised our dual-virus approach where VSV Δ 51 delivers the HER2T while the targeted therapeutic becomes a genetic payload in the counterpart virus, VV. Following intratumoural injection of the viruses, the targeted therapy, the TCE in this approach, becomes locally secreted and sequestered in the tumour to ensure efficacy, while also reducing the probability of off-target adverse events.

Selection of VV as the complementary virus to the target-delivering VSV Δ 51 was based on our previous work modelling the rational design of a superior VSV Δ 51 variant³⁰. The work culminated in the generation of VSV Δ 51 encoding a VV type I interferon decoy receptor⁸, that can promote infection of cancer cells³¹. Here we demonstrated notable synergy between the two backbone viruses (Supplementary Fig. 6); we hypothesize this synergy is mediated through the B19R interferon decoy receptor produced by VV which dampens antiviral responses against VSV Δ 51 in our combination strategy. This combination leads to enhanced VSV Δ 51 spread and overall efficacy, and is safe, well-tolerated, and tumour-localized in vivo (Supplementary Fig. 6e). It is important to note that in the context of VSV Δ 51-HER2T+VV- α HER2-TCE, the limiting factor is the HER2T target, because the TCE is required only in picomolar concentrations to elicit therapeutic efficacy^{32,33}. We observed significant spread of VSV Δ 51-HER2T within tumours, especially when co-injected with VV (Supplementary Fig. 1i), with relatively minimal spread of VV. Therefore due to its faster lifecycle and potential to spread, VSV Δ 51 was selected to propagate the HER2T target, while VV was used to deliver the TCE.

The design of our TCE construct and its insertion into oncolytic VV was based on previous work⁷, although here we utilized the trastuzumab CDR and the vaccinia B19R-competent Tian Tan strain containing the interferon decoy receptor. Combining VSV Δ 51-HER2T and VV- α HER2-TCE, we observed robust T-cell activation in ex vivo patient tumour samples co-cultured with exogenous T-cells (Fig. 3h). In vivo experimentation with this oncolytic virus combination demonstrated robust efficacy across multiple syngeneic murine tumour models of both localized or disseminated disease, through locoregional or systemic treatment administration. (Figs. 4 and 6). While other groups report the absence of immunologic memory following treatment with TCEs³⁴, it appears encoding TCEs within our acutely inflammatory oncolytic viruses does indeed enable the establishment of memory responses, consistent with our previous findings⁷ (Figs. 4 and 5). While we reported modest T-cell activation in ex vivo studies with the VV- α HER2-TCE monotherapy in patient specimens, it should be noted that

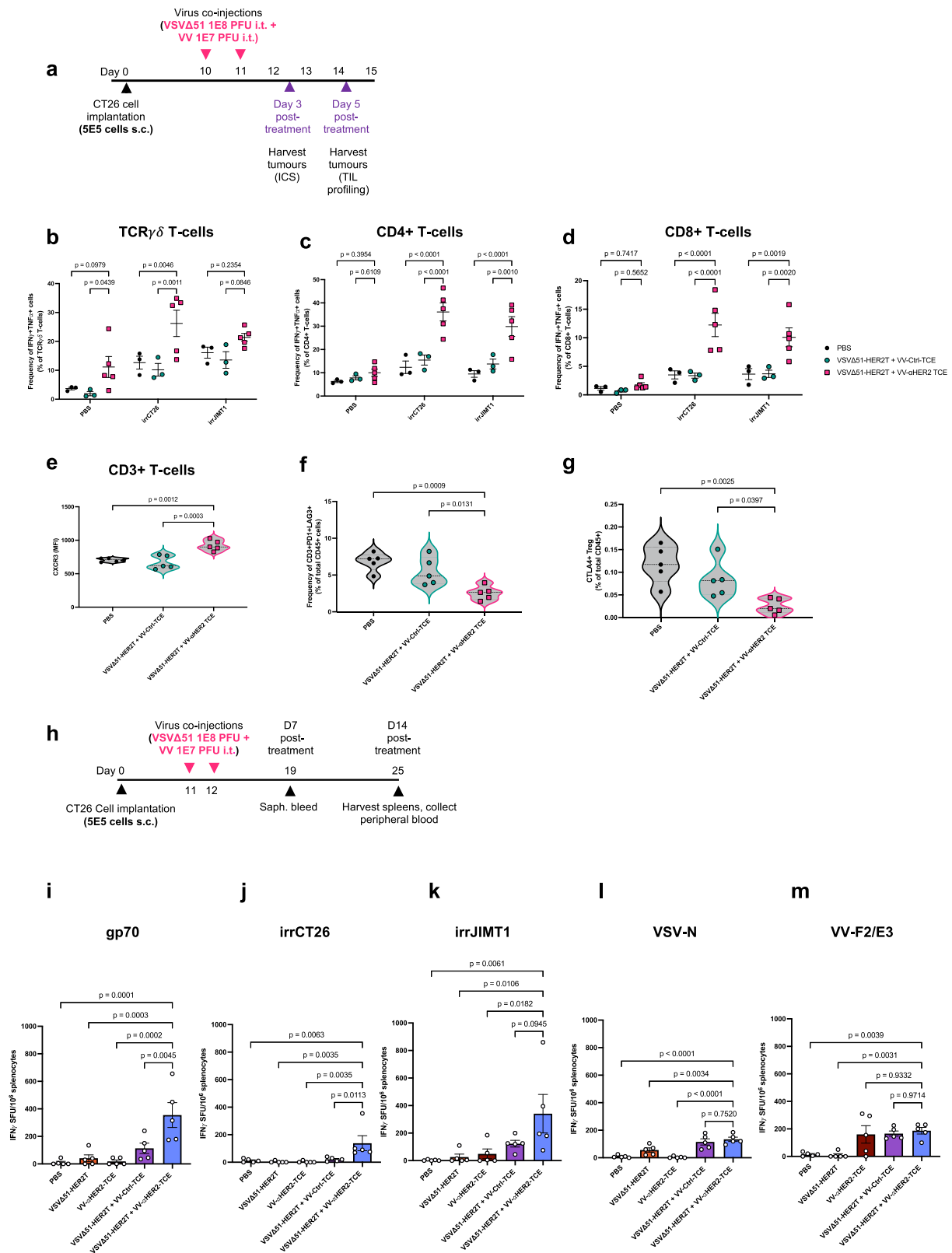
these samples had unknown HER2 status and thus may express HER2. Nonetheless in vivo survival studies confirm that VV- α HER2-TCE yields no survival benefit in HER2- tumours unless co-administered with the cognate VSV Δ 51-HER2T. These results were thus attributable to the rational combination of the therapeutic genetic payloads as indicated by the comparative lack of efficacy in the control groups.

To assess mechanisms of cell death with tumours, we performed histological examination of tumours within 48 hpi following a single intratumoural injection of VSV Δ 51-HER2T+VV- α HER2-TCE and identified distinct highly infected regions (Supplementary Fig. 12). Within these ROI we observed an elevated frequency of cleaved caspase-3 positive cells, indicative of apoptosis and consistent with previous findings on TCE-induced apoptosis⁷. We moreover observed an increase in the frequency of cleaved caspase-1 staining in all ROI co-infected with VSV Δ 51-HER2T and VV, including in the control combination. Here, cleaved caspase-1 is suggestive of inflammasome-mediated pyroptosis, a highly immunogenic and inflammatory mode of cell death triggered by the viral infection^{35–38}.

Overall, we observe an enhancement in both mechanisms of cell death following tumour injection with VSV Δ 51-HER2T+VV- α HER2-TCE. This elevation in positive staining of cell death markers is unsurprisingly localized to infected ROI. We reported a relatively low proportion of infected tumour cells across all tumours, up to 4% by VSV Δ 51-HER2T or up to 1% by VV. Interestingly we observed that tumours infected with VSV Δ 51-HER2T+VV- α HER2-TCE exhibited fewer co-infected cells than tumours infected with the control combination, likely a result of co-infected cells expressing both HER2T and α HER2-TCE being rapidly eliminated. Nonetheless, the minor proportion of infected cells within treated tumours, and by extension the areas of active cell death, could not alone account for the overall efficacy observed.

We therefore investigated early and late anti-tumour immune responses. Within 3–5 days post-injection, we noted significant reactivity of TILs in VSV Δ 51-HER2T+VV- α HER2-TCE treated mice against tumour cells and upregulated migratory markers, compared with controls (Fig. 5). By 14 days post-injection, mice treated with VSV Δ 51-HER2T+VV- α HER2-TCE exhibited robust cell-mediated anti-tumour reactivity, as well as humoral anti-tumour reactivity (Fig. 5h–m, Supplementary Figs. 15 and 16). Immune responses were detected against both endogenous tumour antigen (gp70) and exogenous antigens (HER2T and viral antigens). Together these data implicate a systemic anti-tumour immune response in the efficacy observed following administration of the dual-virus therapy.

This systemic immune response likely drives the therapeutic efficacy observed in the disseminated disease models evaluated (Fig. 6, Supplementary Fig. 17), as well as the anti-tumour immunity responsible for graft rejection following tumour-rechallenge in cured mice (Fig. 4). We acknowledge however that the extent of anti-tumour immunity naturally varies between tumour models and mouse background. For example, we did not observe graft rejection of parental MC38 tumours in rechallenge experiments in cured mice, but only observed rejection of MC38-HER2T tumours (Fig. 4d, e). This finding suggests our dual-virus strategy may have induced an anti-HER2T immune response more potent than a broadly anti-tumour response in this specific model. Alternatively, anti-tumour immunity in this model may have waned within the 90-day waiting period prior to rechallenge.



Our immunological studies were therefore conducted in the CT26 tumour model in BALB/c mice, the same model in which we observed complete graft rejection of both parental CT26 and HER2T-expressing tumours following tumour rechallenge in cured mice (Fig. 4i, j). These rechallenge data are consistent with immunological data revealing the installment of anti-tumour immune responses against endogenous tumour antigens as well as the delivered HER2T antigen (Fig. 5).

Although therapeutic virus combinations are rarely explored, one important example exists in the field of vaccinology: the measles, mumps, and rubella (MMR) vaccine consisting of three live-attenuated viruses, safely administered to children³⁹. Notably, we and others have demonstrated that both viral vectors used as oncolytics are independently safe for immunization against different diseases^{40,41}; vaccinia virus has been employed for smallpox eradication and modern

Fig. 5 | Intratumoural injection of VV- α HER2-TCE and VSV Δ 51-HER2T induces anti-tumour immune responses. **a** Experimental overview: 5×10^5 CT26 cells were implanted s.c. in BALB/c mice in the right flank. Mice were treated i.t. as indicated. Tumours were harvested on day 3 for intracellular staining (ICS) of cytokines, and on day 5 for assessing the profiles of the immune infiltrating populations. **b–d** Following tumour-dissociation, immune cells were cultured ex vivo for 24 h and Golgi plugged following stimulation with PBS control, 2×10^6 irradiated CT26 cells, or 2×10^6 irradiated JIMT1 cells. Immune cells were analysed by flow cytometric analysis for intracellular levels of IFN γ and TNF α in **b** TCR $\gamma\delta$ T-cells, **c** CD4+ T-cells, and **d** CD8+ T-cells. (mean \pm SEM, $n = 3$ mice in PBS and VSV Δ 51-HER2T+VV-Ctrl-TCE groups, $n = 5$ mice in VV- α HER2-TCE+VSV Δ 51-HER2T group; P -value calculated by one-way ANOVA relative to VV- α HER2-TCE+VSV Δ 51-HER2T, with Dunnett correction for multiple comparisons). **e–h** Tumours dissociated at day 5 were analysed by flow cytometric analysis. **e** Levels of CXCR3 (MFI)

in total CD3+ T-cells are shown. Frequency of **(f)** PD1+LAG3+CD3+ T-cells and **(g)** CTLA4+ Tregs were determined relative to total CD45+ cells. For all violin plots, $n = 5$ mice per group; P -value calculated by one-way ANOVA relative to VV- α HER2-TCE+VSV Δ 51-HER2T, with Dunnett correction for multiple comparison.

h Experimental overview: 5×10^5 CT26 cells were implanted s.c. in BALB/c mice in the right flank. Mice were treated i.t. as indicated. Following harvest and dissociation of spleens at D14 post-treatment, splenocytes were subjected to cultured in an ELISpot plate to quantify IFN γ -secreting cells following 16 h culture in the presence of the following stimulation **(i–m)**: $10 \mu\text{M}$ gp70 peptide, irradiated CT26 cells, irradiated JIMT1 cells, $10 \mu\text{M}$ VSV-N peptide, $10 \mu\text{M}$ VV-F2/E3 peptides (mean \pm SEM, $n = 5$ mice per group; P -value calculated by one-way ANOVA relative to VSV Δ 51-HER2T+VV- α HER2-TCE, with Dunnett correction for multiple comparisons). Source data are provided as a Source Data file.

immunization against monkeypox, while VSV has been engineered to immunize against Ebola. Nonetheless, future studies will assess safety of our dual-virus combination in non-human primates, as we have previously done^{40,41}. As mitigation strategies for any unforeseen off-target toxicity, we can potentially employ the use of anti-viral treatments as kill-switches⁴², or even a recently identified small-molecule drug for our HER2-targeting TCE⁴³.

The dual-virotherapy approach developed in this study offers a promising solution to the limitations of precision medicine in cancer treatment. Our strategy overcomes the dependence on specific tumour biomarkers and may remove barriers to candidacy for potent targeted therapies. We demonstrated that this approach elicits a broad anti-tumour immune response with the potential for a clinically feasible single-shot treatment (Figs. 5 and 6, Supplementary Fig. 10), and is therapeutically relevant when administered in the adjuvant setting (Supplementary Fig. 17). Further development and optimization of this approach, including the design of unique antibody-antigen pairs using artificial intelligence^{44–46}, could enhance its clinical applicability and impact on cancer therapy.

Methods

Ethics

In vivo experiments were performed via The Ottawa Hospital Research Institute (OHRI) protocols OHRI-2265 and OHRI-2264, which are in good standing with the Animal Care Committee at the University of Ottawa, and care and treatment of animals was in accordance with the ethical standards of the Canadian Council on Animal Care and with the Animals for Research Act. For all in vivo mouse experiments, the maximal tumour volume allowed was 1500 mm^3 . In some cases, this limit has been exceeded the last day of measurement and the mice were immediately euthanized. Animals were also euthanized if they exhibited signs of unwellness, all according to the institutional guidelines review board for animal care.

Consenting of patients for specimen collection was done by the treating surgeon at the time of consent for surgery, as part of the standard procedure at The Ottawa Hospital. These specimens were collected as part of the Platform of Global Consenting for Tissue (GTC) from Surgical Specimens, under the protocol OHSN REB # 20180079-01 and 20220124-01H, approved by the OHRI Research Ethics Board, with no compensation for patient participation.

Cells

All cell lines used, growth media, vendors, and catalogue numbers are listed in Supplementary Table 3. [†]These lines were generated as previously described⁶. [‡]69 cells were generated by CRISPR-mediated insertion of TdTomato under the control of the CD69 promoter in Jurkat cells⁷. All media were supplemented with 10% foetal bovine serum (VWR, Mississauga, Ontario, Canada, Cat. # 45001-106) and 1% penicillin-streptomycin solution (ThermoFisher Scientific, Cat. # 15140163), unless otherwise indicated. All cells were maintained at

37°C in a 5% CO_2 humidified incubator, routinely tested for mycoplasma contamination by Hoechst staining and PCR (Diamed, Mississauga, Ontario, Catalogue # ABMG238) and used within 3–10 passages since thaw. None of the cell lines listed were present in the commonly misidentified cell lines database maintained by ICLAC. The HER2T+ cell lines used to generate the immune-competent mouse models of human HER2T+ cancer are available upon request by contacting Dr. Jean-Simon Diallo (jsdiallo@ohri.ca).

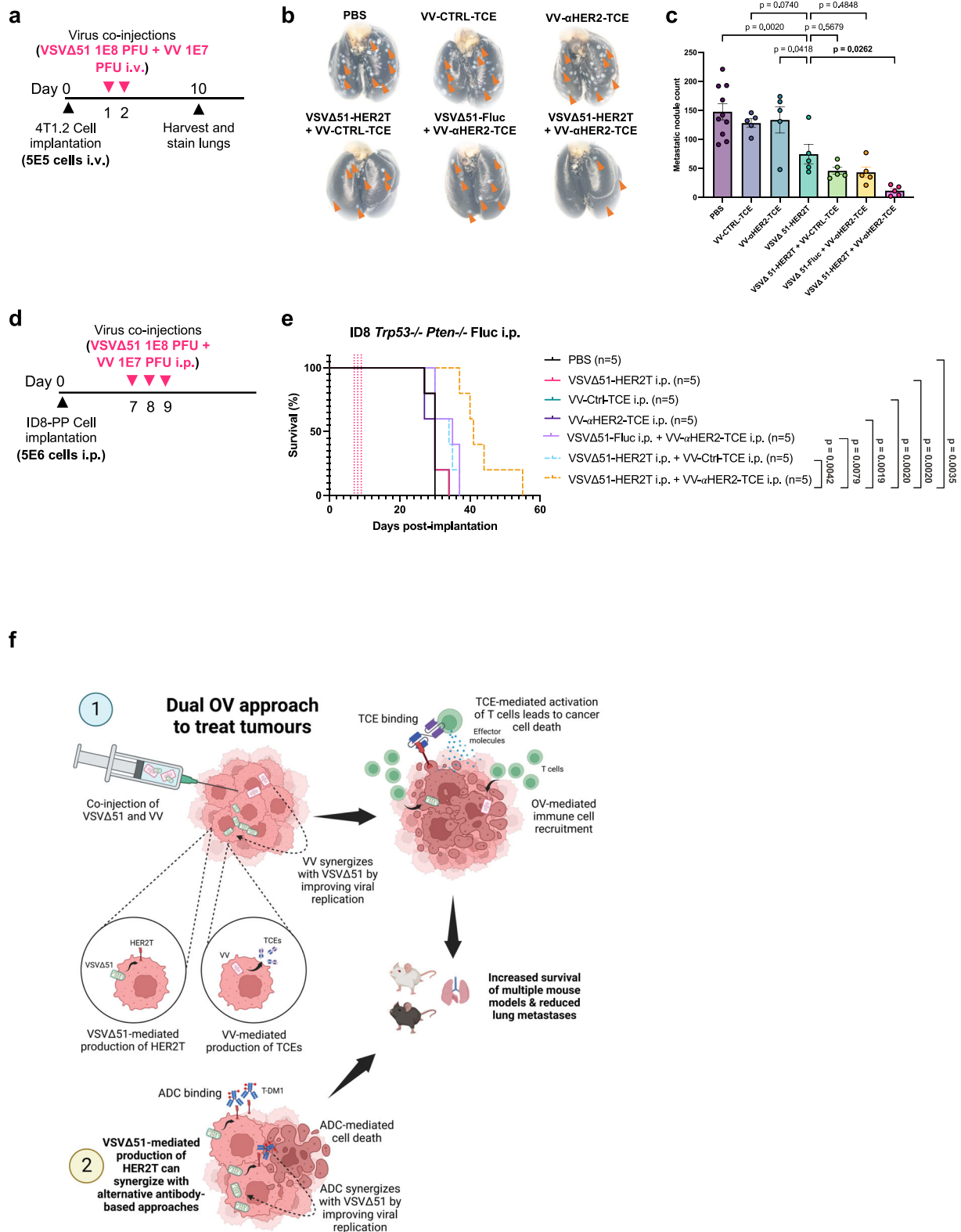
Plasmids

TCE constructs were created using sequences from the EMBL-EBI database and IMGT database for anti-human CD3 (OKT3) and anti-murine CD3 (145-2C11) single-chain variable fragments (scFv), respectively, in addition to the trastuzumab HER2 sequence. A flexible glycine-serine (GS) linker was utilized to connect the two scFv fragments. The TCE sequences were designed to include a Kozak sequence and an Ig κ leader sequence for secretion. A C-terminal His-tag was included for TCE detection. Plasmids were synthesized (GenScript, NJ, USA). Through restriction enzyme digestion, TCEs were cloned into a vaccinia vector for insertion into the B14R locus along with EGFP and Fluc reporter transgenes.

To generate VSV Δ 51-HER2T, the expression plasmid encoding human wildtype ERBB2 (NM_004448.3) was obtained as a gift from Mien-Chie Hung (Addgene plasmid # 16257; <http://n2t.net/addgene:16257;RRID:Addgene16257>). The required truncations were generated, and the *HER2T* cds⁶ was amplified by PCR. The final amplicon was flanked by 5' XhoI and a 3' NheI cutsites for insertion into the gene junction between *G* and *L* in the VSV Δ 51 backbone. The sequence for HER2T in VSV Δ 51-HER2T is distinct from the sequence of HER2T used in the generation of stable HER2T+ cell lines.

TCE expression

Transfection of HEK293T cells with TCE-pcDNA was performed in a 15 cm^2 plate. A total of $20 \mu\text{g}$ DNA and $60 \mu\text{l}$ Lipofectamine 2000 were used, following the manufacturer's instructions (Life Technologies, ON, CAN). OptiMEM (ThermoFisher Scientific) was used as the transfection medium, and cells were incubated at 37°C with 5% CO_2 for 6 h. Subsequently, the transfection mixture was replaced with serum-free DMEM, and the cells were further incubated for 48 h at 37°C with 5% CO_2 . To concentrate the TCEs, supernatants from the transfected cells were collected and cleared of cell debris by centrifugation at $400 \times g$ for 5 min at room temperature. The resulting supernatants were then subjected to centrifugal concentration using Amicon Ultra-15 Centrifugal Filter Units with a 10 kDa molecular weight cutoff (EMD Millipore, Cat. # UFC901024, MA, USA). This step involved centrifugation at $4500 \times g$ for 30 min at 4°C . The concentrated TCE samples were aliquoted and stored at -80°C until further use. Quantification of TCEs was performed utilizing a pre-coated anti-His ELISA kit (Cayman Chemical, Cat. # 10012445, MI, USA) following the manufacturer's instructions.



Viruses

Vaccinia virus (VV). The parental VV Tian Tan strain was previously described⁴⁰. To propagate oncolytic VV, HeLa cells were cultured in roller bottles of 1700 cm², using DMEM supplemented with 25 mM HEPES. These cells were infected with the virus at a multiplicity of infection (MOI) of 0.05 and incubated at 37 °C until the development of a cytopathic effect (48–72 h). The resulting viruses were harvested and purified following established protocols^{40,47}. Viral titres were

quantified by standard plaque assay titration using U-2 OS cells, as described^{7,40,47}.

Generation of VV-TCE. Insertion of αHER2 TCE transgenes derived from TCE-pcDNA plasmids was achieved by integrating them into a VV expression backbone (VV-TCE plasmid) containing homology arms specific to the vaccinia B14R locus. Standard DNA cloning techniques involving XhoI and NotI restriction enzymes (NEB) for digestion and

Fig. 6 | Treatment of tumour-bearing mice with VV- α HER2-TCE and VSV Δ 51-HER2T prolongs overall survival and reduces lung metastases in disseminated disease models. **a** Experimental overview: 5×10^5 4T1.2 cells were injected i.v. by tail vein injection into BALB/c mice, and treated as indicated, followed by harvest and staining of lungs. **b** Following staining with black India ink, lungs were fixed and imaged. **c** Metastatic lung nodules were quantified. Shown are mean \pm SEM, $n = 10$ mice in the PBS group, $n = 5$ mice in all other groups; P -value calculated by one-way ANOVA relative to VSV Δ 51-HER2T, with Dunnett correction for multiple comparisons. **d** Experimental overview: 5×10^6 ID8-PP cells were implanted i.p. in C57BL/6 mice, followed by treatments as indicated. **e** Overall survival was monitored; P -values indicated next to treatment groups is relative to VSV Δ 51-HER2T+VV- α HER2-TCE. For analysis of survival data, P -values were calculated by the Kaplan–Meier method followed by log-rank test. Source data are provided as a Source Data file. **f** Schematic depicting the dual oncolytic virus approach to treat tumours (indicated

by the number 1), whereby VSV Δ 51 and VV produce the HER2T synthetic target and its cognate TCE, respectively. These two OVVs synergize since VV dampens interferon levels and increases VSV Δ 51 replication. VV-produced TCEs recognize and bind to HER2T, forming a pseudo-immunological synapse that allows for the release of effector molecules (e.g. granzyme, perforin). OVVs lead to the recruitment of immune cells in the tumour, and TCEs mediate the activation of T cells that trigger apoptosis of cancer cells. Ultimately, this strategy improves survival of mice bearing different tumour types and decreases lung metastases. Importantly, VSV Δ 51-mediated production of HER2T on the surface of cancer cells can synergize with other alternative antibody-based approaches, such as antibody-drug conjugates like T-DMI (indicated by the number 2). In this case, the ADC can synergize with VSV Δ 51 to promote viral replication. The ADC-mediated cell death also leads to increased survival in preclinical animal models and decreased lung metastases in mice.

ligation were utilized during this process, and the resulting constructs were verified through sequencing. TCE expression was regulated by both pEarly and pLate promoters. The coding sequence (cgs) for Fluc and the fluorescent selection marker EGFP were separated by a P2A sequence, and their expression was also under the control of pEarly and pLate promoters. U-2 OS cells were infected with parental Tian Tan vaccinia virus at a multiplicity of infection (MOI) of 0.05 for 2 h. Subsequently, the media was removed, and the cells were transfected with 1 μ g of DNA, maintaining a DNA-to-Lipofectamine 2000 ratio of 1:3. After 2 h, the transfection mix was replaced with DMEM supplemented with 10% foetal bovine serum (FBS). Recombination facilitated the insertion of TCE transgenes into the viral genome. The infected cells were incubated for 48 h at 37 °C with 5% CO₂ and examined for EGFP expression. For virus rescue, cells showing EGFP-positive plaques were collected and subjected to three cycles of freeze/thawing. The collected virus was serially diluted and used to infect fresh U-2 OS cells. The newly infected U-2 OS cells were cultured with an overlay medium composed of a 1:1 mixture of 3% carboxymethyl cellulose (CMC) and 2 \times DMEM supplemented with FBS for 48 h at 37 °C with 5% CO₂. Plaques displaying EGFP-positive signals were selected using sterile pipette tips, and three rounds of freeze/thawing were performed. The resulting virus was used to infect U-2 OS cells in subsequent iterations of the process until pure virus was obtained. Once a pure virus population was established, an mCherry geneblock was introduced into the J2R locus using U-2 OS Cas9 cells and an sgRNA guide targeting the locus, following previously described methods⁴⁸. Selection for double-positive plaques expressing EGFP-mCherry was performed.

Vesicular stomatitis virus (VSV Δ 51). The oncolytic versions of VSV (Indiana serotype) encoding a firefly luciferase protein tag (VSV Δ 51-Fluc), green fluorescent protein (VSV Δ 51-GFP) tag, red fluorescent protein (VSV Δ 51-RFP) tag, or truncated HER2 (VSV Δ 51-HER2T) were propagated using Vero cells as previously described⁴⁹. Briefly, VSV Δ 51 was added at an MOI of 0.01 to 95% confluent Vero cells in 150 mm culture dishes or roller bottles in a total volume of 25 ml complete DMEM. Inoculated Vero cells were incubated at 37 °C with 5% CO₂ for 24 h or until approximately 50% CPE (cytopathic effects, cell rounding) was observed. Supernatants were collected and pelleted at 780 g to clear heavy debris. Virus contained within the cleared supernatant was subsequently subject to 0.22 μ m membrane filtration and purified using 5–50% OptiPrep (Sigma-Aldrich, Oakville, ON, Canada, Cat. # D1556) gradient. The purified virus suspension was aliquoted and frozen at –80 °C. For all virus infections, viruses were diluted in serum free DMEM to obtain the specified multiplicity of infection (MOI), or for mock infection cells were supplemented with an equal volume of serum free DMEM.

For quantification of viral titres by using standard plaque assay titration, Vero cells were seeded into 12-well plates at a final density of 3×10^5 cells per well. Infectious supernatants were serially diluted using serum-free DMEM, transferred (500 μ L/well) onto Vero cells and

incubated at 37 °C, 5% CO₂ for 45 min. Media was removed and replaced with 1 ml/well of an agarose overlay (1:1 ratio of 1% agarose mixed with 2 \times DMEM containing 20% FBS). After a 24 h incubation, plaques were fixed with methanol: glacial acetic acid in a 3:1 ratio for a minimum of 1 h, then stained for 30 min with a Coomassie Blue solution (Sigma, Cat. # B0149; 4 g Coomassie Brilliant Blue R, 800 ml methanol, 400 ml acetic acid and 2800 ml distilled water) to visualize and count plaques.

Quantification of viral infection by reporter imaging. Virus infections were conducted on cells cultured in serum-free media at the designated multiplicities of infection (MOIs). After a 1.5–2 h incubation period, the media were replaced with RPMI or DMEM supplemented with 10% FBS and 1% (*v/v*) penicillin/streptomycin. Following incubation at 37 °C in 5% CO₂, cells were examined for EGFP or RFP expression at 24 or 48 hpi using an EVOS M5000 fluorescence microscope (Thermo Fisher Scientific) or Cellomics ArrayScan (Thermo Fisher Scientific) using the HCS Studio v2 software.

For the treatment of Vero cells by IFN β (AVNONEX™, Interferon beta-1a) cells were seeded in 96- or 24-well plates. Cells were treated with IFN β at the indicated concentrations for 30 min, followed by co-infection with VSV Δ 51-RFP and/or VV at the indicated MOI.

Viral growth curves. Cells were seeded in 24 well plates for overnight confluency. Cells were then inoculated with VSV Δ 51 or VV at an MOI of 0.01 (multi-step growth curve) or 1.0 (single-step growth curve). Cells infected at MOI 1.0 were incubated for 60 min, following by washing and replenishing with fresh medium.

For VSV Δ 51, cells were incubated up to 54 hpi, with the supernatant collected and frozen in Eppendorf tubes at –80 °C at the indicated timepoints. For VV, cells were incubated up to 72 hpi. Cells were scraped off each well and collected and frozen with the supernatant in Eppendorf tubes at –80 °C at the indicated timepoints. Viral titre in collected supernatant was quantified by standard plaque assay.

Immunoblotting

Samples were prepared following protein quantification via a bicinchoninic acid assay (ThermoFisher Scientific, Cat. # 23227; Waltham, MA, USA), and immunoblotting was performed with equal amounts of protein for whole cell lysates or supernatant samples. Total protein was detected by ponceau S staining (Sigma-Aldrich, Cat. # P7170-1L; St Louis, MO, USA). TCEs were detected via their His tag using a mouse anti-His antibody (Abcam, 1:1000, Cat.# ab18184, ON, Toronto, Canada). Vaccinia virus presence was confirmed with a rabbit polyclonal antibody that detects vaccinia virus proteins (LSBio, Cat. # LS-C103289, 1:1000, Seattle, WA, USA). HER2 levels were detected using a mouse monoclonal antibody against human HER2/ErbB2 (1:1000, Invitrogen, Cat. # MA5-13105). β -Actin (1:1000; 13E5; Cell Signalling Technology) was used as a loading control for immunoblots. After overnight incubation with primary antibodies, the immunoblots

were probed with HRP-coupled anti-rabbit or anti-mouse antibodies (1:5000) (Jackson ImmunoResearch Laboratory, West Grove, PA, USA, Cat. # 711-035-152 (anti-rabbit) 715-035-150 (anti-mouse)). Supersignal West Pico Plus Chemiluminescent substrate (Thermo Scientific, Cat. # 34577, Burlington, Ontario, Canada,) was used to visualize the protein bands on a Bio-Rad ChemiDoc.

Metabolic activity assay

The metabolic activity of cells was evaluated using alamarBlue (Invitrogen, Cat. # DAL1025, MA, USA) or resazurin sodium salt (Sigma-Aldrich, Cat. # R7017) following the manufacturer's instructions. Treated and/or infected cells were treated with 10% (*v/v*, final) resazurin in each well and incubated for 1–2 h, depending on the specific cell line. Fluorescence intensity was measured at 590 nm upon excitation at 530 nm using the BioTek Synergy or Cytation 5 Microplate Readers (BioTek, VT, USA).

TCE or antibody binding assay

Single-cell suspensions (5×10^5 cells) were placed on ice and treated with His-tagged TCEs or trastuzumab (10–25 $\mu\text{g}/\text{ml}$) for 1 h prior to washing away excess unbound TCEs or antibody. Anti-His IgG-Alexa-Fluor 647 (1:300, ThermoFisher Scientific, Cat. # MA1-21315-A647) or anti-human IgG-PE (1:500, Invitrogen, Cat. # PA1-86978) were used to quantify attachment to cell-surface. Fluorescence was quantified by Cytation 5 plate reader (Biotek). MFI were normalized to mock control MFI.

Syngeneic mouse models

For cell implantation into mice, cells were washed twice with PBS, filtered through a 70 μm filter, and counted using ViCell. The cells were then resuspended in PBS and kept on ice until the injection procedure. Tumours were implanted by mixing equal volume of cells with cold Geltrex[®] (1:1 ratio, Thermo Fisher, Cat. # A1413201). After tumour implantation, animal cohorts were randomized before the initiation of treatment regimens. Tumour volumes were determined using a modified ellipsoidal formula: $Tumour\ volume = \frac{width^2 \times length}{2}$, where width corresponds to the smallest dimension. For palpable tumours, mice were treated when tumours reached 80–100 mm^3 as indicated in figures. Mice were euthanized when tumour volumes reached above 1500 mm^3 , and according to the institutional guidelines review board for animal care. Tumour progression was regularly monitored by measurements every other day, or every 2 days. As such, there were instances where maximum tumour volumes were marginally exceeded.

For all in vivo mouse experiments, female mice were used to account for the relevance of breast cancer and ovarian cancer models used, as well as to account for sex-based physiological variability. Using female mice further enabled minimization of animal housing costs ($n = 5$ per cage) compared to male mice ($n = 1$ per cage).

In 8-week-old female immunocompetent C57BL/6 mice (Charles River Laboratories, Wilmington, MA, USA), MC38 (or MC38-HER2T) murine colorectal cancer cells (5×10^5 cells in 50 μL of PBS), or B16-F10 (5×10^5 cells in 50 μL of PBS) murine melanoma cells were injected subcutaneously. Alternatively, ID8 *Tp53*^{-/-} *Pten*^{-/-} Fluc (ID8-PP) (or ID8-PP-HER2T) murine ovarian cancer cells (5×10^6 cells in 50 μL of PBS) were injected intraperitoneally into the abdomen. Treatment with viruses or controls was administered at the designated time points.

Bioluminescence imaging by IVIS Spectrum (Living Image Software v4.7) (PerkinElmer, Waltham, MA, USA) was performed on ID8-PP i.p. tumour-bearing mice for longitudinal monitoring of tumour burden. Mice were imaged one a week for a total of four weeks. Briefly, 200 μL of 10 mg/ml D-luciferin (PerkinElmer, Cat. # 1227991) were injected subcutaneously in mice, which were rested for 5 min. Mice were then anesthetized by inhaled isoflurane, imaged using a 30 s

exposure, then revived. Radiance and total flux were calculated using the Living Image v4.7 software (PerkinElmer).

8-week-old female immunocompetent BALB/c mice (Charles River Laboratories, Wilmington, MA, USA), 4T1.2 (or 4T1.2-HER2T) murine breast cancer cells or CT26 (or CT26-HER2T) murine colorectal cancer cells (5×10^5 cells in 50 μL of PBS) were injected subcutaneously. Alternatively, 4T1.2 cells (5×10^5 cells in 50 μL of PBS) were injected intravenously into the tail veins of mice for the lung metastasis model. Treatment with intravenous injections of viruses or controls was administered at the indicated time points prior to lung harvesting. On day 10, mice were euthanized, and their lungs were injected intratracheally with black India ink. The lungs were then excised, rinsed with water, and fixed in Fekete solution (100 mL formalin, 700 mL ethanol, 50 mL glacial acetic acid, and 150 mL distilled water) before counting the metastatic nodules.

All rechallenge studies were performed D90 post-implantation, by implanting bilateral tumours. For these bilateral implantations, cells were seeded at double the original seeding density, distal or contralateral to the initial site of tumour implantation. Parental tumours were implanted in the contralateral side, while HER2-expressing derivatives of the parental tumours were implanted in the right flank at a distal site from the initial tumour. Tumour progression and overall survival were monitored over time.

Post-surgical metastasis model

8-week-old female immunocompetent C57BL/6 mice were implanted orthotopically with B16-F10 cells (5×10^5 cells) subcutaneously in the right flank. 10 days post implantation when tumours reached 150–250 mm^3 and were given enough time to disseminate metastatic cells, tumours were surgically excised. Mice were observed in post-operative care for 24 h. 48 h following recovery, mice received intravenous injections of the indicated treatments via tail vein. Animals were monitored for wellness until day 45 following initial implantation. All primary tumours, lungs, and spleens were collected. Each animal was scored 0–3 as indicated in Supplementary Fig. 17b, where recurrence of the primary tumour = +1, spleen metastasis = +1, lung metastasis = +1.

Tracking migration of i.v. injected tumour cells

Confirmation of migration of i.v. 4T1.2 cell injection to lungs was done by IVIS fluorescence imaging. Briefly, 4T1.2 cells were stained with IVISense DiR 750 Fluorescent Cell Labelling Dye (Revvity, Cat. # 125964, MA, USA) according to the manufacturer's instructions. Cells were then injected into mice through tail veins. Following 1 h and 24 h post-injection, ventral sides of mice were imaged by IVIS (EX710/EM760). Following imaging, mice were euthanized, lungs were perfused with a total volume of 10 ml of PBS supplemented with 50 IU/ml heparin sodium salt through slow injection (200 $\mu\text{L}/\text{s}$) into the right ventricle. Lungs were then inflated by slow (200 $\mu\text{L}/\text{s}$) instillation of 10% neutral buffered formalin solution for overnight fixation. Lungs were then processed for hematoxylin and eosin staining for subsequent histological analysis for the identification of micrometastatic lesions.

Virus biodistribution

Female BALB/c mice bearing CT26 tumours were injected with i.t. VSV Δ 51 or VSV Δ 51 + VV at the indicated doses. 48 hpi, mice were euthanized. Organs and tumours were harvested and snap frozen for subsequent RNA extraction. Frozen tissues were crushed using a dounce homogenizer; RNA extraction was performed by using QiaShredder columns (Qiagen, Cat. # 79656, Hilden, Germany) and RNeasy kits (Qiagen, Cat. # 74106). RNA was converted to cDNA using (Thermo Fisher Scientific, Cat. # K1622). Real-time PCRs were performed using PowerUp[™] SYBR[™] green, according to the manufacturer's instructions (Thermo Fisher Scientific, Cat. # A25776) on a 7500 Fast Real-Time PCR system (Applied Biosystems). Optimal

thresholds, reaction efficiencies, and Ct values were determined using the ABI software and melt curves for each primer exhibited a single peak. Gene expression relative to HPRT was calculated by the Pfaffl method. Fold-change was determined relative to the Mock control for each gene. Primers used:

VSV-N F: GATAGTACCGGAGGATTGACG
VSV-N R: TCAAACCATCCGAGCCATTC
mHPRT F: TGAAGAGCTACTGTAATGATCAGTCAA
mHPRT R: AGCAAGCTTGAACCTTAACCA

Bilateral CT26 model for intratumoural viral spread

8-week old female BALB/c mice were implanted with s.c. CT26 tumours in both the left and right flanks. 11 days post-implantations when tumour volumes reach ~100–150 mm³, both tumours were injected as indicated. Mice were euthanized and tumours were collected at either 24 or 48 h post-injection. All tumours from the right flank were dissociated as described below. All tumours from the left flank were fixed in 10% neutral buffered formalin solution for subsequent paraffin embedding, sectioning, and immunohistochemistry.

Xenograft mouse models

8-week-old female CD1 nude mice (CrI:CD1-Foxn1^{nu}; Charles River Laboratories, Wilmington, Massachusetts, USA, Strain code # 086) were implanted subcutaneously with HT-29 human colorectal cancer cells (5×10^5 cells in 100 μ L of PBS). Prior to implantation, cells were mixed with equal volume of cold Geltrex[®] (1:1 ratio, Thermo Fisher).

Tissue processing

Tumours were dissociated using the Miltenyi mouse tumour dissociation kit (Miltenyi Biotec, Cat. # 130-096-730, CA, USA) and the gentleMACS Octo Dissociator (Miltenyi Biotec, Cat. # 130-096-427). Spleens were collected and dissociated by crushing the organs through a 70 μ m strainer using the plunger of a 3 mL syringe. All dissociated spleens underwent erythrocyte lysis using ACK buffer (Gibco, Cat. # A1049201). All cell suspensions were strained and counted. 2×10^6 cells were resuspended in 200 μ L of FACS buffer (0.5% BSA-PBS) and transferred to round-bottom 96-well plates for staining for flow cytometry. Alternatively, dissociated tumours or splenocytes were resuspended in 100 μ L RPMI supplemented with 10% heat-inactivated FBS for in vitro culture.

Flow cytometry

After processing tissues as described above, cells were stained with fixable viability dye FVS510 (1:1000, BD Biosciences, NJ, USA, Cat. #564406) in PBS for 15 min at room temperature. Cells were washed and then incubated with anti-CD16/32 (1:100, BD Biosciences, Cat. # 553141) in 0.5% BSA-PBS for 30 min at 4 °C to block non-specific antibody interaction with Fc receptors. Cells were next incubated with CellBlox[™] blocking buffer (1:100, Invitrogen, Cat. # B001T06F01) to block non-specific interactions with monocytes and macrophages. Cells were subsequently stained with an antibody cocktail diluted in 0.5% BSA-PBS and Super Bright complete staining buffer (1:50, Invitrogen, Cat. # SB-4401-75). Antibodies are detailed in Supplementary Table 4. Cells were then washed and resuspended in 1% paraformaldehyde (PFA) in PBS. Samples were acquired with the BD LSRFortessa[™] (using FACS Diva[™] v9 software) or the Cytex[®] Aurora spectral cytometer (using SpectroFlo[®] software) at the University of Ottawa Flow Cytometry and Virometry core facility (Director: Dr. Vera Tang), and the OHRI Flow Cytometry and Cell Sorting core facility (Director: Fernando Ortiz). Data were analysed using FlowJo v10.8 software or the OMIQ online platform. Dimensionality reduction plots were generated using the opt-SNE⁵⁰. Unstained controls, and fluorescence-minus-one (FMO) controls were prepared in parallel. Ultracomp eBeads (Thermo Scientific, Cat. # 01-2222-42) single-stained beads were used for compensation.

For the detection of virally-encoded fluorophores, samples were not fixed and were assessed by flow cytometry immediately after dissociation and staining to prevent fluorescence quenching. For the detection of cells infected by VSVΔ51-HER2T, cells were stained with trastuzumab (1:1000) followed by a goat anti-human IgG-PE (1:300, Invitrogen, PA1-86078).

Intracellular staining

Dissociated tumour specimens, including tumour-infiltrating lymphocytes, were counted and seeded at 1×10^6 cells in 100 μ L RPMI supplemented with 10% FBS, 10 mM HEPES, 50 μ M 2-mercaptoethanol, and $1 \times$ non-essential amino acids (Gibco, Cat. #11140050) in round-bottom 96-well plates. Cells were incubated with 100 μ L of the following stimulants for 4 h: PBS, irradiated CT26 cells, irradiated JIMT1 cells, 10 μ M VSV-N peptide (H-2Ld MPYLIDFGL⁵¹, CanPeptide Inc.), 10 μ M VV-F2/E3 peptides SPGAAGYDL/VGSPNSPTF⁵²; Genscript, NJ, USA), 10 μ M gp70 (AH1) peptide (H-2Ld SPSVYHQF⁵¹, MBL International Corporation, Cat. # SPM521), or PMA (50 ng/ml) and ionomycin (1 μ g/ml) (BioLegend, Cat. # 423301). GolgiPlug/Brefeldin A (1:1000, BD Biosciences, Cat. # 555029) was added to each well, and cells were incubated overnight for 18 h. Cells were stained for viability and surface markers, followed by fixation and permeabilization (BD Cytofix/Cytoperm[™], BD BioSciences, Cat. # 554714). Intracellular staining was performed according to the protocol previously described. Antibodies are detailed in Supplementary Table 4.

For the preparation of irradiated stimulants, CT26 or JIMT1 cells were resuspended in CTL medium (Immunospot, Cat. # CTLT-010, OH, USA) at 2×10^6 cells per 100 μ L, then irradiated (Pantak HF320 X-Ray Machine) with 90 Gy.

Mouse IFN- γ single-colour enzyme-linked immune absorbent spot (ELISPOT)

ELISpots were done as previously described⁶. Briefly, Immunospot ELISPOT plates were prepared according to manufacturer's instructions (Immunospot, OH, USA, Cat. # mIFN γ -1M/5), with stimulants added to wells as indicated. 2×10^5 splenocytes incubated in CTL medium in the IFN- γ pre-coated plates. Spots were counted using ImmunoSpot[®] Software version 5.3. Counts from unstimulated/DMSO control were treated as background and subsequently subtracted from all conditions within the same sample. Stimulants used were: DMSO, irradiated CT26 cells, irradiated JIMT1 cells, 10 μ M VSV-N peptide, 10 μ M VV-F2/E3 peptides, 10 μ M gp70 (AH1) peptide, or PMA (50 ng/ml) and ionomycin (1 μ g/ml) (BioLegend, Cat. # 423301). For irradiation, cells were resuspended in CTL medium at 2×10^6 cells per 100 μ L, then irradiated (Pantak HF320 X-Ray Machine) with 90 Gy.

IgG assay

3×10^5 cells were resuspended in 100 μ L of 0.5% BSA-PBS and transferred to a round-bottom 96-well plate. Cells were incubated with mouse serum (1:100) for 60 min. at 4 °C, then incubated with goat anti-mouse IgG-AlexaFluor[™] Plus 488 (1:300, Invitrogen, Cat. # A32723). Cells were washed and resuspended in 1% PFA-PBS and acquired by flow cytometry.

Ex vivo tumour cores

Mouse tumours were excised immediately after mice were euthanized. Patient specimens were retrieved from the pathology lab after patient consenting and surgical excision. Smaller patient specimens were exhausted, and higher priority conditions received as many tumour cores as possible, leaving few cores for lower priority conditions (such as $n = 2$ cores in Fig. 3h; Basal cell carcinoma and Ovarian samples, VV-Ctrl-TCE control condition). All tumours were trimmed and processed into 2 mm thick sections, which were then cored by 2 mm punch biopsy (Integra Miltex, VWR, Cat. # 21909-132). Cores were cultured in DMEM supplemented with 10% FBS, 10 mM HEPES, 0.75 μ g/ml amphotericin B, 1% penicillin-streptomycin, and 50 μ g/ml gentamicin

in 24-well plates. Cores were treated as indicated, and infected with 3×10^6 PFU/core VSVΔ51 or 3×10^5 PFU/core VV.

For the J69 activation assay, cores were infected as described. 48 hpi J69 were added (1×10^6 cells/well) and incubated for 24 h. J69 cells were then dislodged from the well, collected, and analysed by flow cytometric analysis for TdTomato signal.

Immunofluorescence (IF) staining

Cells on sterile glass coverslips were incubated overnight at 37 °C. Cells were then fixed with 4% paraformaldehyde, quenched with 100 mM glycine in PBS* (supplemented with 1 mM CaCl₂ and 0.5 mM MgCl₂), and blocked in 5% BSA-PBS*. For detection of cell surface HER2 or HER2T, slides were incubated overnight at 4 °C with trastuzumab (1:1000), in 1% BSA-PBS*. Coverslips were washed then incubated for 1 h at room temperature with a goat anti-human IgG-AlexaFluor-594 (1:200, Invitrogen, Cat. # A-11014). Coverslips were mounted on slides with ProLong Diamond anti-fade with DAPI (Invitrogen, Cat. # P36962), and stored at 4 °C. Images were taken using the AxioCam HRm camera (Carl Zeiss Ltd, Toronto ON) mounted on the Zeiss AxioScope Imager M1 or the Zeiss Axio Imager M2 microscope. Image analysis and signal quantification was performed using ImageJ v2.9 software.

Immunohistochemistry (IHC)

For frozen tissue samples: following harvest, tumours were rinsed with PBS then embedded and frozen in O.C.T. medium using an ethanol dry ice bath. Samples were sectioned by cryostat and mounted. Slides were gradually thawed at room temperature before brief rehydration with PBS followed by fixation with 4% paraformaldehyde. Serially sectioned slides were blocked with serum-free Dako protein block (Agilent, Cat. # X090930-2, CA, USA). Tissue sections for intracellular VSV detection were permeabilized for 10 min in a solution of 0.2% Triton-X100 in PBS*. Sections for extracellular HER2 or HER2T detection were not permeabilized. Staining was done using rabbit polyclonal anti-VSV^{53,54} (1:5000) or trastuzumab (1:1000) overnight, followed by visualization using anti-rabbit IgG-Alexa Fluor-594 (1:300, Invitrogen, Cat. # A-11012) or anti-human IgG-Alexa Fluor-594 (1:300, Invitrogen, Cat. # A-11014). Slides were mounted using ProLong Diamond anti-fade with DAPI (Invitrogen, Cat. # P36962), and imaged using a Zeiss Axio Imager M2 microscope and ZEN v2.6 (blue edition) software.

For fixed tissue samples: following harvest, tumour samples were rinsed in PBS and fixed in 10% neutral buffered formalin (Sigma, Cat. # HT501128) for 24 h, then transferred to 70% ethanol. Following paraffin embedding and sectioning, 4 μm thick tissue sections were deparaffinized (5 min each in CitriSolv™ (DeconLabs, Cat. # 1601, PA, USA) then rehydrated in descending alcohol series (100%, 95%, 90%, 80%, 5 min each). Antigen retrieval was performed in citrate buffer (pH 6.0, Vector H-3301) and endogenous peroxidase activity was quenched in 3% H₂O₂. Tissue sections were blocked using serum-free Dako protein block. Serially sectioned slides were then incubated with the following primary antibodies overnight at 4 °C: rabbit anti-vaccinia virus polyclonal antibody (1:2000, Invitrogen, Cat. # PA1-7258), rabbit anti-VSV polyclonal antibody^{53,54} (1:2000), rabbit anti-cleaved caspase 1 monoclonal antibody (1:500, Invitrogen, Cat. # PA5-99390), rabbit anti-cleaved caspase 3 monoclonal antibody (1:2000, Cell Signalling Technology, Cat. # 9664). Slides were developed using the ImmPRESS HRP Horse Anti-rabbit IgG Kit (Vector Laboratories, Cat. # MP-7401-15), then counterstained in hematoxylin, dehydrated, and mounted. Tissue sections were imaged using an AxioScan.Z1 and the ZEN v2.6 (blue edition) software. For quantification of 3,3'-Diaminobenzidine (DAB) staining, percentage of DAB-positive cells were calculated in per ROI per section, using QuPath v0.5.1 software⁵⁵.

Statistics and reproducibility

All graphs and statistical analyses were performed using Excel or GraphPad Prism v.10.2.1. Individual statistical tests were detailed in

figure legends. A minimum of three biological replicates are used in all experiments. Each in vitro or ex vivo experiment was independently replicated a minimum of twice. All animal experiments were replicated in multiple models, by 2 different operators. All in vitro experiments are the result of at least 2 independent experiments. One-way or two-way ANOVA were followed-up with Fisher's LSD test when few planned comparisons were pre-determined. Exact *P*-values are indicated where possible, but are capped at a lower limit of *P* = 0.0001 for ANOVA when calculated using GraphPad Prism. Normal distribution of the data was assessed using D'Agostino & Pearson omnibus and Shapiro–Wilk normality tests. Non-parametric tests were implemented if assumptions for parametric tests were not met. Alpha levels for all tests were 0.05 (confidence levels of 95%). Analysis of in vivo survival data was performed by the Kaplan–Meier method followed by log-rank test. In vivo group sizes were based on a power calculation of 0.8, with an anticipated doubling of mOS. The number of ex vivo tumour core biological replicates was based on a power calculation of 0.8, with an anticipated tripling in viral titre, or an anticipated doubling in J69 activation. Power calculations were computed using the NIH Sample Size Calculator⁵⁶. Biological replicates are indicated by a number *n*, and defined as per NIH guidelines, and error calculated as the standard error of the mean (SEM).

Reporting summary

Further information on research design is available in the Nature Portfolio Reporting Summary linked to this article.

Data availability

Source data are provided with this paper. All data are available within the Article, Supplementary Information or Source Data file, Source data are provided with this paper.

References

1. Finck, A., Gill, S. I. & June, C. H. Cancer immunotherapy comes of age and looks for maturity. *Nat. Commun.* **11**, <https://doi.org/10.1038/s41467-020-17140-5> (2020).
2. Arulanandam, R. et al. The strategic combination of trastuzumab emtansine with oncolytic rhabdoviruses leads to therapeutic synergy. *Commun. Biol.* **3**, 254 (2020).
3. von Minckwitz, G. et al. Trastuzumab Emtansine for Residual Invasive HER2-Positive Breast Cancer. *N. Engl. J. Med.* **380**, 617–628 (2019).
4. Cortés, J. et al. Trastuzumab Deruxtecan versus Trastuzumab Emtansine for Breast Cancer. *N. Engl. J. Med.* **386**, 1143–1154 (2022).
5. Swain, S. M., Shastry, M. & Hamilton, E. Targeting HER2-positive breast cancer: advances and future directions. *Nat. Rev. Drug Discov.* **22**, 101–126, (2023).
6. Taha, Z. et al. Syngeneic mouse model of human HER2+ metastatic breast cancer for the evaluation of trastuzumab emtansine combined with oncolytic rhabdovirus. *Front. Immunol.* **14**, 1181014 (2023).
7. Crupi, M. J. F. et al. Oncolytic virus driven T-cell-based combination immunotherapy platform for colorectal cancer. *Front. Immunol.* **13**, 1029269 (2022).
8. Le Boeuf, F. et al. Synergistic interaction between oncolytic viruses augments tumor killing. *Mol. Ther.* **18**, 888–895 (2010).
9. Arulanandam, R. et al. Microtubule disruption synergizes with oncolytic virotherapy by inhibiting interferon translation and potentiating bystander killing. *Nat. Commun.* **6**, 6410 (2015).
10. Lücke, J. et al. Protocol for generating lung and liver metastasis in mice using models that bypass intravasation. *STAR Protoc.* **5**, 102696 (2024).
11. Rashid, O. et al. Is tail vein injection a relevant breast cancer lung metastasis model? *J. Thorac. Dis.* **5**, 385–392 (2013).
12. Li, G. et al. CD3 engagement as a new strategy for allogeneic “off-the-shelf” T cell therapy. *Mol. Ther. Oncolytics* **24**, 887–896 (2022).

13. Morita, M., Mizui, M., Masuyama, S., Tsokos, G. C. & Isaka, Y. Reduction of Cell Surface T-Cell Receptor by Non-Mitogenic CD3 Antibody to Mitigate Murine Lupus. *Front. Immunol.* **13**, 855812 (2022).
14. Reits, E. A. et al. Radiation modulates the peptide repertoire, enhances MHC class I expression, and induces successful anti-tumor immunotherapy. *J. Exp. Med.* **203**, 1259–1271 (2006).
15. Belkina, A. C. et al. Automated optimized parameters for T-distributed stochastic neighbor embedding improve visualization and analysis of large datasets. *Nat. Commun.* **10**, 5415 (2019).
16. Mateo, J. et al. Delivering precision oncology to patients with cancer. *Nat. Med.* **28**, 658–665 (2022).
17. Choi, B. D. et al. CAR-T cells secreting BiTEs circumvent antigen escape without detectable toxicity. *Nat. Biotechnol.* **37**, 1049–1058 (2019).
18. Aalipour, A. et al. Viral Delivery of CAR Targets to Solid Tumors Enables Effective Cell Therapy. *Mol. Ther. Oncolytics* **17**, 232–240 (2020).
19. Park, A. K. et al. Effective combination immunotherapy using oncolytic viruses to deliver CAR targets to solid tumors. *Sci. Transl. Med.* **12**, eaaz1863 (2020).
20. Liu, Y. et al. Oncolytic herpes simplex virus delivery of dual CAR targets of CD19 and BCMA as well as immunomodulators to enhance therapeutic efficacy in solid tumors combined with CAR T cell therapy. *Front. Oncol.* **12**, 1037934 (2022).
21. Zhang, A. Q. et al. Universal redirection of CAR T cells against solid tumours via membrane-inserted ligands for the CAR. *Nat. Biomed. Eng.* <https://doi.org/10.1038/s41551-023-01048-8> (2023).
22. Heinrich, M. et al. Suicide risk and mortality among patients with cancer. *Nat. Med.* **28**, 852–859 (2022).
23. Hurvitz, S. A. et al. Trastuzumab deruxtecan versus trastuzumab emtansine in patients with HER2-positive metastatic breast cancer: updated results from DESTINY-Breast03, a randomised, open-label, phase 3 trial. *Lancet* **401**, 105–117 (2023).
24. Li, B. T. et al. Trastuzumab Deruxtecan in HER2-Mutant Non-Small-Cell Lung Cancer. *N. Engl. J. Med.* **386**, 241–251 (2022).
25. Modi, S. et al. Trastuzumab Deruxtecan in Previously Treated HER2-Positive Breast Cancer. *N. Engl. J. Med.* **382**, 610–621 (2020).
26. Gamboa, L. et al. Sensitizing solid tumors to CAR-mediated cytotoxicity using synthetic antigens. Preprint at <https://doi.org/10.21203/rs.3.rs-1276779/v1>.
27. Breitbach, C. J. et al. Oncolytic vaccinia virus disrupts tumor-associated vasculature in humans. *Cancer Res.* **73**, 1265–75 (2013).
28. Arulanandam, R. et al. VEGF-Mediated Induction of PRD1-BF1/Blimp1 Expression Sensitizes Tumor Vasculature to Oncolytic Virus Infection. *Cancer Cell* **28**, 210–224 (2015).
29. Breitbach, C. J. et al. Targeting tumor vasculature with an oncolytic virus. *Mol. Ther.* **19**, 886–894 (2011).
30. Le Boëuf, F. et al. Model-based rational design of an oncolytic virus with improved therapeutic potential. *Nat Commun* **4**, 1974 (2013).
31. Bastin, D. et al. Enhanced susceptibility of cancer cells to oncolytic rhabdo-virotherapy by expression of Nodamura virus protein B2 as a suppressor of RNA interference. *J. Immunother. Cancer* **6**, 62 (2018).
32. Crupi, M. J. F., Bell, J. C. & Singaravelu, R. Concise Review: Targeting Cancer Stem Cells and Their Supporting Niche Using Oncolytic Viruses. *Stem Cells* **37**, 716–723 (2019).
33. Scott, E. M., Duffy, M. R., Freedman, J. D., Fisher, K. D. & Seymour, L. W. Solid Tumor Immunotherapy with T Cell Engager-Armed Oncolytic Viruses. *Macromolecular Biosci.* **18**, <https://doi.org/10.1002/mabi.201700187> (2018).
34. Benonisson, H. et al. CD3-bispecific antibody therapy turns solid tumors into inflammatory sites but does not install protective memory. *Mol. Cancer Ther.* **18**, 312–322 (2019).
35. Ma, J. et al. Characterization of virus-mediated immunogenic cancer cell death and the consequences for oncolytic virus-based immunotherapy of cancer. *Cell Death Dis.* **11**, 48 (2020).
36. Wang, Y. et al. Inflammasome Activation Triggers Caspase-1-Mediated Cleavage of cGAS to Regulate Responses to DNA Virus Infection. *Immunity* **46**, 393–404 (2017).
37. Yu, P. et al. Pyroptosis: mechanisms and diseases. *Sig. Transduct. Targeted Ther.* **6**, <https://doi.org/10.1038/s41392-021-00507-5> (2021).
38. Denes, A., Lopez-Castejon, G. & Brough, D. Caspase-1: Is IL-1 just the tip of the ICEberg? *Cell Death Dis.* **3**, <https://doi.org/10.1038/cddis.2012.86> (2012).
39. Ohn, J. et al. Safe administration of the measles vaccine to children allergic to eggs. *N. Engl. J. Med.* **332**, 1262–1266 (1995).
40. Boulton, S. et al. Single-dose replicating poxvirus vector-based RBD vaccine drives robust humoral and T cell immune response against SARS-CoV-2 infection. *Mol. Ther.* **30**, 1885–1896 (2022).
41. Boulton, S. et al. A T Cell-Targeted Multi-Antigen Poxvirus Vector Vaccine Generates Robust Cellular and Humoral Immunity Against SARS-CoV-2 Infection. *Mol. Ther. Methods Clin. Dev.* 101110 <https://doi.org/10.1016/j.omtm.2023.101110> (2023).
42. Wang, J. et al. An Overview of Antivirals against Monkeypox Virus and Other Orthopoxviruses. *J. Med. Chem.* **66**, 4468–4490 (2023).
43. Gong, N. et al. Small-molecule-mediated control of the anti-tumour activity and off-tumour toxicity of a supramolecular bispecific T cell engager. *Nat. Biomed. Eng.* <https://doi.org/10.1038/s41551-023-01147-6> (2024).
44. Jumper, J. et al. Highly accurate protein structure prediction with AlphaFold. *Nature* **596**, 583–589 (2021).
45. Ruffolo, J. A., Chu, L.-S., Mahajan, S. P. & Gray, J. J. Fast, accurate antibody structure prediction from deep learning on massive set of natural antibodies. *Nat. Commun.* **14**, 2389 (2023).
46. Davila, A. et al. AbAdapt: an adaptive approach to predicting antibody-antigen complex structures from sequence. *Bioinformatics Adv.* **2**, vbac015 (2022).
47. Martin, N. T. et al. Engineering Rapalog-Inducible Genetic Switches Based on Split-T7 Polymerase to Regulate Oncolytic Virus-Driven Production of Tumour-Localized IL-12 for Anti-Cancer Immunotherapy. *Pharmaceuticals* **16**, 709 (2023).
48. Whelan, J. T. et al. CRISPR-mediated rapid arming of poxvirus vectors enables facile generation of the novel immunotherapeutic STINGPOX. *Front. Immunol.* **13**, 1050250 (2023).
49. Diallo, J. S., Vähä-Koskela, M., Le Boeuf, F. & Bell, J. Propagation, purification, and in vivo testing of oncolytic vesicular stomatitis virus strains. In *Methods in Molecular Biology* vol. 797 127–140 (Humana Press Inc., 2012).
50. Belkina, A. C. et al. Automated optimized parameters for T-distributed stochastic neighbor embedding improve visualization and analysis of large datasets. *Nat. Commun.* **10**, 1–12 (2019).
51. Alluqmani, N. et al. Vanadyl sulfate-enhanced oncolytic virus immunotherapy mediates the antitumor immune response by upregulating the secretion of pro-inflammatory cytokines and chemokines. *Front. Immunol.* **13**, 1032356 (2022).
52. Boulton, S. et al. A T cell-targeted multi-antigen vaccine generates robust cellular and humoral immunity against SARS-CoV-2 infection. *Mol. Ther. Methods Clin. Dev.* **31**, 101110 (2023).
53. Breitbach, C. J. et al. Targeting Tumor Vasculature With an Oncolytic Virus. *Mol. Ther.* **19**, 886 (2011).
54. Wedge, M. E. et al. Virally programmed extracellular vesicles sensitize cancer cells to oncolytic virus and small molecule therapy. *Nat. Commun.* **13**, 1–16 (2022).
55. Bankhead, P. et al. QuPath: Open source software for digital pathology image analysis. *Sci. Rep.* **7**, 1–7 (2017).
56. Kohn, M. A. & Senyak, J. NIH Sample Size Calculator. *UCSF CTSI* <https://www.sample-size.net/> (Accessed 03 April 2024) (2024).

Acknowledgements

We thank members of the Diallo, Bell, and Ilkow labs for feedback and support on this project. We would like to thank the team of technicians at

the Ottawa Hospital Cancer Centre Pharmacy for providing Kadcyla and Herceptin. We thank Dr. Guy Ungerechts for providing MC38 cells. ID8 *Tp53*^{-/-} *Pten*^{-/-} cells were generated by CRISPR Cas9-mediated knock-out and were generously provided by Dr. Iain McNeish. Primary human ovarian cancer cells (AF2028, AF2068, AF2780) were obtained from the Ottawa Ovarian Ethics Board (OHSN-REB 1999540-01H) with informed consent, and provided by Dr. Barbara Vanderhyden. Collection of human tissue/fluid for this study was made possible by the Global Tissue Consent and Collection Program at the OHRI (Tissue Navigator: Edita Delic; OHSN REB # 20180079-01 and 20220124-01H). We acknowledge the use of instruments and expertise from the University of Ottawa Flow Cytometry Core Facility, which is funded by the University of Ottawa, Natural Sciences and Engineering Research Council of Canada, and the Canadian Foundation for Innovation. We also acknowledge the assistance of Fernando Ortiz from the Flow Cytometry & Cell Sorting Facility at OHRI for facility management. The authors acknowledge the Cell Biology and Image Acquisition Core (RRID: SCR_Q21845) funded by the University of Ottawa, Ottawa, Natural Sciences and engineering Research Council of Canada, and the Canada Foundation for Innovation. We thank the personnel of the Louise Pelletier Histology Core (RRID: SCR_Q21737), and Animal Care and Veterinary Service of the Faculty of Medicine at the University of Ottawa for their support. All pre-clinical bioluminescent imaging (IVIS) was done at the University of Ottawa Preclinical Imaging Core (RRID:SCR_Q21832). The following figures were created using BioRender.com, released under a Creative Commons Attribution-NonCommercial-NoDerivs 4.0 International license: Fig. 1a, Fig. 1b, Fig. 2a, Fig. 2i, Fig. 6f, Supplementary Fig. 2a, Supplementary Fig. 5a, Supplementary Fig. 5b, and Supplementary Fig. 8a. J.-S.D. is supported by the CIHR New Investigator Award-Infection and Immunity (INI-147824), funding from the Terry Fox Research Institute, TFF-122868, Canadian Institutes of Health Research, grant 705952, a Canadian Cancer Society grant supported by the Lotte & John Hecht Memorial Foundation, grant #703014. This research was also funded by a Canadian Cancer Society Impact (#706162) grant to J.C.B. and C.S.I., and co-applicant M.J.F.C., as well as grants to J.C.B. and C.S.I. from the Canadian Institutes of Health Research (#377104), and generous support from the Ontario Institute for Cancer Research, the Ottawa Regional Cancer Foundation, and the Ottawa hospital foundation. Z.T. was supported by a NSERC doctoral award CGS-D3, Mitacs CanPrime and Accelerate fellowships, Ontario Graduate Scholarship, Queen Elizabeth II Graduate Scholarship in Science and Technology (QEII-GSST), and a Canadian Cancer Society Research Training Award – PDF level (CCS award 708044). M.J.F.C. was funded by the Taggart-Parkes Fellowship, as well as a Mitacs CanPRIME Accelerate and a Mitacs Elevate fellowship. N.A. is supported by a scholarship from King Faisal Specialist Hospital and Research Center, Riyadh, Saudi Arabia (KFSHRC) representative by Saudi Arabian Cultural Bureau in Canada (SACB). A.A. is supported by a doctoral scholarship from Umm AlQura University, Saudi Arabia. S.V. and D.A.T. were funded by a CIHR CGS-M and a Mitacs CanPrime accelerate. S.V. was also funded by the Ontario Women’s Health Scholar (OWHS) Award and OGS. J.T.W., P.R.B., and T.K.H.L. were funded by a Mitacs CanPrime accelerate. K.N. and J.S. were supported by a BioCanRx Undergraduate Studentship. V.H.G. was funded by an Ontario Graduate Scholarship. S.B. was funded by a CIHR Postdoctoral fellowship and Mitacs Elevate fellowship.

Author contributions

Z.T., M.J.F.C., J.-S.D., J.C.B. participated in conceptualization and methodology design of the studies. J.-S.D., J.C.B., C.S.I. provided supervision, guidance, and funding acquisition for the project. Z.T., M.J.F.C., N.A.,

J.T.W., B.Z.H., O.K., D.A.T., R.M., M.H., S.M. performed in vitro investigation. Z.T., M.J.F.C., N.A., S.V., J. Pe, M.T., A.C., M.M.S., C.T.d.S., J. Po, S.B., V.H.G. performed and assisted with in vivo animal investigation. Z.T., M.J.F.C., N.A. performed flow cytometry preparation and acquisition. Z.T., M.J.F.C., N.A., S.V. performed immunohistochemical (IHC) staining and imaging. Z.T. and D.M. performed IHC image analyses. F.F. performed scoring and evaluation of lung sections. Z.T. and M.J.F.C. performed formal analyses. Z.T. and M.J.F.C. performed data visualization, and project administration. Z.T., M.J.F.C., A.A., K.N., J.S., P.R.B., T.K.H.L., D.A.T. performed validation experimentation. Z.T., M.J.F.C., N.A., A.C., M.H. propagated, purified, and validated VSVΔ51. M.J.F.C., J.T.W., R.M., B.Z.H., O.K. propagated, purified, and validated VV. Z.T., and M.J.F.C. prepared the original manuscript with editorial contributions from J.S.-D., R.A., J.C.B., and C.S.I..

Competing interests

Z.T., M.J.F.C., J.C.B., J.-S.D. report having a pending patent directly related to this work entitled “Delivery vehicles expressing engineered antigens and uses thereof” (U.S. Provisional Patent Application No. 63/680, 672). The other authors declare no competing interests.

Additional information

Supplementary information The online version contains supplementary material available at <https://doi.org/10.1038/s41467-024-51498-0>.

Correspondence and requests for materials should be addressed to Zaid Taha, Mathieu Joseph François Crupi, John Cameron Bell or Jean-Simon Diallo.

Peer review information *Nature Communications* thanks Anastasia Lipatova, Richard Vile and the other, anonymous, reviewer(s) for their contribution to the peer review of this work. A peer review file is available.

Reprints and permissions information is available at <http://www.nature.com/reprints>

Publisher’s note Springer Nature remains neutral with regard to jurisdictional claims in published maps and institutional affiliations.

Open Access This article is licensed under a Creative Commons Attribution-NonCommercial-NoDerivatives 4.0 International License, which permits any non-commercial use, sharing, distribution and reproduction in any medium or format, as long as you give appropriate credit to the original author(s) and the source, provide a link to the Creative Commons licence, and indicate if you modified the licensed material. You do not have permission under this licence to share adapted material derived from this article or parts of it. The images or other third party material in this article are included in the article’s Creative Commons licence, unless indicated otherwise in a credit line to the material. If material is not included in the article’s Creative Commons licence and your intended use is not permitted by statutory regulation or exceeds the permitted use, you will need to obtain permission directly from the copyright holder. To view a copy of this licence, visit <http://creativecommons.org/licenses/by-nc-nd/4.0/>.

© The Author(s) 2024

¹Centre for Cancer Therapeutics, Ottawa Hospital Research Institute, Ottawa, ON K1H 8L6, Canada. ²Department of Biochemistry, Microbiology, and Immunology, Faculty of Medicine, University of Ottawa, Ottawa, ON K1H 8M5, Canada. ³Department of Pathology and Molecular Medicine, McMaster University, Hamilton, ON, Canada. ⁴Cancer Immunology Team, National Research Council of Canada, Human Health Therapeutics, Ottawa, ON K1A 0R6, Canada. ⁵These authors contributed equally: Zaid Taha, Mathieu Joseph François Crupi. ⁶These authors jointly supervised this work: John Cameron Bell, Jean-Simon Diallo. ✉ e-mail: ztaha053@uottawa.ca; mcrupi@ohri.ca; jbelle@ohri.ca; jsdiallo@ohri.ca